materials

MDPI

Review

Deformation Mechanisms and Processing Maps for High Entropy Alloys (Presentation of Processing Maps in Terms of Zener–Hollomon Parameter): Review

Hee-Tae Jeong and Woo Jin Kim *

Department of Materials Science and Engineering, Hongik University, Mapo-gu, Sangsu-dong 72-1, Seoul 121-791, Republic of Korea
* Correspondence: kimwj@hongik.ac.kr

Abstract: In this review paper, the hot compressive deformation mechanisms and processing maps of high-entropy alloys (HEAs) with different chemical compositions and crystal structures are analyzed. The stress exponent (n_1) values measured from the series of compression tests for the HEAs performed at different temperatures and strain rates are distributed between 3 and 35, and they are most populated between 3 and 7. Power law breakdown (PLB) is found to typically occur at $T/T_m \leq 0.6$ (where T is the testing temperature and T_m is the melting temperature). In $Al_xCrMnFeCoNi$ (x = 0–1) and $Al_xCrFeCoNi$ (x = 0–1) HEAs, n_1 tends to decrease as the concentration of Al increases, suggesting that Al acts as a solute atom that exerts a drag force on dislocation slip motion at high temperatures. The values of activation energy for plastic flow (Q_c) for the HEAs are most populated in the range between 300 and 400 kJ/mol. These values are close to the activation energy of the tracer diffusivity of elements in the HEAs ranging between 240 and 408 kJ/mol. The power dissipation efficiency (η) of the HEAs is shown to follow a single equation, which is uniquely related to n_1. Flow instability for the HEAs is shown to occur near n_1 = 7, implying that the onset of flow instability occurs at the transition from power law creep to PLB. Processing maps for the HEAs are demonstrated to be represented by plotting η as a function of the Zener–Hollomon parameter ($Z = \exp(\frac{Q_c}{RT})$, where R is the gas constant). Flow stability prevails at $Z \leq 10^{12}$ s^{-1}, while flow instability does at $Z \geq 3 \times 10^{14}$ s^{-1}.

Keywords: high-entropy alloys; hot compression; deformation mechanisms; processing maps

check for updates

Citation: Jeong, H.-T.; Kim, W.J. Deformation Mechanisms and Processing Maps for High Entropy Alloys (Presentation of Processing Maps in Terms of Zener–Hollomon Parameter): Review. *Materials* **2023**, *16*, 919. https://doi.org/10.3390/ma16030919

Academic Editor: Lijun Zhang

Received: 1 December 2022
Revised: 8 January 2023
Accepted: 12 January 2023
Published: 18 January 2023

1. Introduction

High-entropy alloys (HEAs) are a new family of solid-solution alloys made of four or more principal alloying elements alloyed in equiatomic or near-equiatomic concentrations (with each constituent element having a concentration from 5 to 35 atomic percent (at.%)) [1,2]. The first approach for designing an HEA was to obtain a single-phase solid solution by maximizing the mixing configurational entropy, but later, new design approaches involving multiple phases and/or intermetallics were explored [1–3].

Thermomechanical working at high temperatures is necessary not only to form and shape materials into components but also to produce the desired microstructures and properties of products [4,5]. For this reason, the high-temperature deformation mechanisms and hot workability of HEAs have been studied [6–100]. Finding the constitutive equations that mathematically depict the material response to the applied hot deformation conditions can be useful in predicting the flow stress or strain rates and identifying the rate-determining deformation mechanisms at different temperatures/strain rates and microstructural parameters. Characterization of hot workability using a processing map is important for the optimization of hot working conditions of materials and fabrication of defect-free components [101]. If a material is processed under unstable flow conditions, adiabatic shear banding or cracking can occur, and if a material is processed under optimal conditions, superior microstructure and mechanical properties can be obtained.

In this work, we have reviewed and analyzed the hot compression data of HEAs available in the literature to elucidate their deformation mechanisms and optimal hot working conditions.

2. History and Materials

The first paper reporting the hot compression behavior of HEAs was available in 2011, and the first studied HEAs were $Nb_{25}Mo_{25}Ta_{25}W_{25}$ and $V_{20}Nb_{20}Mo_{20}Ta_{20}W_{20}$ alloys [6], where the microstructural change during hot compression at temperatures of 1073–1873 K and at a strain rate of 10^{-3} s^{-1} was examined. The papers published in the literature from 2011 to the present can be categorized into three groups (Figure 1a). The first group of papers reports the hot compressive deformation data of the HEAs in the limited temperature and strain rate range. The second group of papers reports the hot compression data of the HEAs in a wide range of temperature and strain rates, but processing maps are not constructed. The third group of papers reports the hot compression data as well as the processing maps of the HEAs. The number of publications increases almost exponentially with time, indicating that attention to this academic and engineering field has rapidly increased.

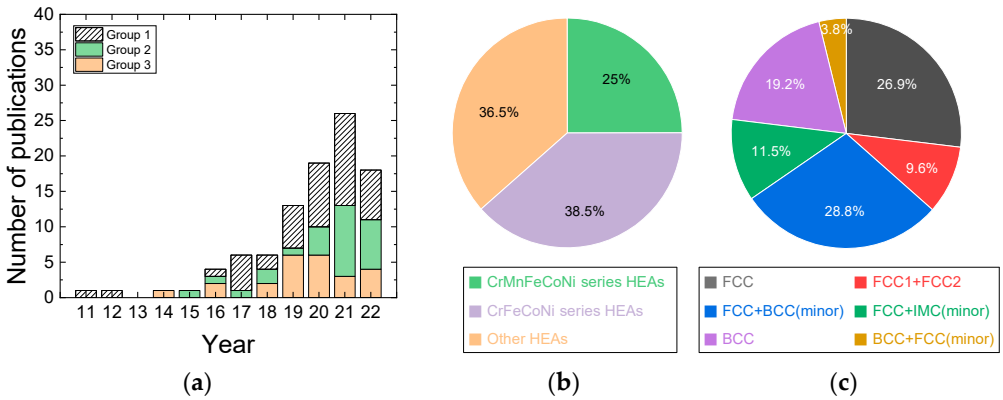

Figure 1. (**a**) Papers published in the literature from 2011 are categorized into three groups. The first group of papers includes papers that report hot compressive deformation of the HEAs in the limited temperature and strain rate range, the second group of papers provides hot compression data of the HEAs over a wide range of temperature and strain rates, but processing maps are not constructed, and the third group of papers provides hot compression data (over a wide range of temperature and strain rates) as well as processing maps of the HEAs. (**b**) Three material groups of HEA materials studied for hot compression, which are classified by their chemical compositions. (**c**) HEA materials studied for hot compression, which are classified by phases (crystal structures).

The HEA materials studied by hot compression can be classified into three groups (Figure 1b). The first material group is the Cr-Mn-Fe-Co-Ni series HEAs containing Al, Sn, Zr, Sn, C, and N [9,20,23,27,34,37,38,42,45,60,62–64]; the second material group is the Cr-Fe-Co-Ni series HEAs containing Zr, Ta, Nb, Mo, Cu, C, and N [13,25,51,53,72,84,92,96,97,100]; and the third material group is the other composition HEAs, including the materials of TiVNbMoTa, $Mn_5Co_{25}Fe_{25}Ni_{25}Ti_{20}$, MnFeCoNiCu, etc. [8,11,12,22,29,32,33,40,41,47,52,56,68,71,74,79,91,93,95,99]. Information regarding the chemical compositions of the HEAs, grain sizes, crystal structure, types of phases, temperature and strain rate ranges for hot compression tests are provided in Table 1. Most of the HEAs studied for hot compression are as-cast or heat-treated (homogenized) cast with coarse grain sizes. Among the Cr-Mn-Fe-Co-Ni series HEAs and Cr-Fe-Co-Ni series HEAs, $Al_xCoCrFeNi$ and $Al_xCoCrFeMnNi$ (x = 0–1) HEAs [9,13,23,25,27,34,42,45,51,53,62,63,71,84,92,96,97,100] have been the most studied, where the addition of Al can facilitate the formation of BCC phase from the FCC matrix. At low Al levels corresponding to x = 0–0.4 or 0.5, the alloys have a single FCC phase, but with a further increase in Al content in the range of x = 0.4 or 0.5–0.9, both FCC

and BCC phases coexist, and at Al addition beyond x = 0.9–0.95, a BCC single phase is obtained [102,103].

Table 1. Information regarding the chemical compositions of the HEAs, grain sizes, crystal structure, types of phases, temperature and strain rate ranges for hot compression tests.

Composition	Grain Size (μm)	Major Phase	Minor Phase	T Range (K)	$\dot{\varepsilon}$ Range (s^{-1})	T_m (K)	n_1	Q_c (kJ/mol)	Material Group
CrMnFeCoNi [9]	300	FCC	-	873–1373	10^{-4}–10^{-2}	1801	4.9–12.1	352.2 (ε_{SS})	1
CrMnFeCoNi [23]		FCC	-	1073–1273	10^{-3}–1	1801	5–8.5	350.5 ($\varepsilon_{0.9}$)	1
CrMnFeCoNi [27]	419	FCC	-	1023–1323	10^{-3}–10	1801	5.8–22.8	410.9 ($\varepsilon_{0.6}$)	1
CrMnFeCoNi [45]	12.8	FCC	-	1023–1423	10^{-3}–10	1801	4.7–11.1	311.9 ($\varepsilon_{0.7}$)	1
$Al_{0.5}$CrMnFeCoNi [34]	547	FCC	BCC	1023–1323	10^{-3}–10	1722	4.2–10.8	343 ($\varepsilon_{0.6}$)	1
$Al_{0.5}$CrMnFeCoNi [62]	547	FCC	BCC	1423&1473	10^{-3}–10	1722	3.6–4.1	570.5 ($\varepsilon_{0.6}$)	1
$Al_{0.7}$CrMnFeCoNi [63]		FCC	BCC	1173–1373	10^{-3}–10	1695	3.2–5.3	309.5 ($\varepsilon_{0.7}$)	1
AlCrMnFeCoNi [42]	118	BCC	-	1173–1373	10^{-3}–10	1657	3.4–5.3	336.3 ($\varepsilon_{0.5}$)	1
CrMnFeCoNi$Sn_{0.5}$ [64]	>100	FCC	$L2_1$	1023–1248	10^{-3}–10	1683	4.6–9.4	322.2 ($\varepsilon_{0.7}$)	1
CrMnFeCoNi$C_{0.5}$ [37]	600	FCC	-	973–1273	10^{-3}–1	1801	8–26	479 ($\varepsilon_{0.6}$)	1
CrMnFeCoNi-1 at.%C [20]	125	FCC	M_7C3	973–1273	10^{-3}–1	1801	8.4–33	605.1 ($\varepsilon_{0.6}$)	1
$(CrMnFeCoNi)_{95}C_5$ [38]	50	FCC	$M_{23}C_6$	1073&1273	10^{-3}–10^{-1}	1801	6.3–10.5	424.1 ($\varepsilon_{0.6}$)	1
$Cr_{25}Mn_{15}Fe_{10}Co_{35}Ni_{15}$ [60]	190	FCC	-	1123–1273	10^{-3}–10^{-1}	1801	5–6.3	310.4 ($\varepsilon_{1.0}$)	1
CrFeCoNi [96]	>100	FCC	-	1173–1373	10^{-3}–10^{-1}	1872	5.8–7	390.1 ($\varepsilon_{0.8}$)	2
$Al_{0.3}$CrFeCoNi [25]	>100	FCC	-	1023–1223	5×10^{-4}–10^{-1}	1806	5.2–9.7	361.4 ($\varepsilon_{0.7}$)	2
$Al_{0.3}$CrFeCoNi [92]	52	FCC	-	1023–1423	10^{-3}–10	1806	4.5–11.1	320.3 ($\varepsilon_{0.7}$)	2
$Al_{0.5}$CrFeCoNi [13]	>100	FCC	BCC	1173–1473	10^{-3}–1	1767	4.4–5.8	296.8 ($\varepsilon_{0.8}$)	2
$Al_{0.5}$CrFeCoNi [13]	>100	FCC	BCC	1223–1373	10^{-3}–1	1767	4.7–4.8	304 ($\varepsilon_{0.8}$)	2
$Al_{0.5}$CrFeCoNi [84]	>100	FCC	BCC	1173–1373	1.3×10^{-3}–10^{-1}	1767	4.7–6.3	361.8 ($\varepsilon_{0.7}$)	2
$Al_{0.6}$CrFeCoNi [53]	>100	FCC	BCC	1173–1473	10^{-3}–1	1749	4.5–6.4	380 ($\varepsilon_{0.6}$)	2
$Al_{0.6}$CrFeCoNi [97]	>100	FCC	BCC	1223–1373	10^{-3}–1	1749	3.7–4.5	287.5 ($\varepsilon_{0.8}$)	2
$Al_{0.7}$CrFeCoNi [72]	>100	FCC	BCC	1173–1373	10^{-3}–10^{-1}	1732	4.1–5.1	375.5 ($\varepsilon_{0.6}$)	2
$Al_{0.7}$CrFeCoNi [100]	>100	FCC	BCC	1073–1373	10^{-2}–10	1732	4.7–6.5	321.3 ($\varepsilon_{0.5}$)	2
AlCrFeCoNi [51]	194	BCC1	BCC2	1073–1373	10^{-3}–1	1684	3.3–4.2	180.6 ($\varepsilon_{0.8}$)	2
$(CrFeCoNi)_{90}Zr_{10}$ [54]	>100	FCC	Ni_2Zr + Ni_7Zr_2	1073–1323	10^{-3}–10	1897	3.9–6.6	327.8 ($\varepsilon_{0.6}$)	2
CrFeCoNi$Ta_{0.395}$ [69]	>100	FCC	Laves	1073–1373	10^{-3}–1	1999	4.1–6.9	383.5 ($\varepsilon_{0.6}$)	2
CrFeCoNi$Nb_{0.25}$ [89]	>100	FCC	Laves	1073–1273	10^{-2}–10	1923	5–9.2	431.9 ($\varepsilon_{0.8}$)	2
CrFeCoNi$Mo_{0.2}$ [18]		FCC	-	973–1373	10^{-3}–1	1921	3.4–20	491.2 ($\varepsilon_{0.6}$)	2
CrFeCoNiCu (as-cast) [90]	>100	FCC1	FCC2	1073–1173	10^{-2}–1	1769	3.4–9.7	374.2 ($\varepsilon_{0.4}$)	2
CrFeCoNiCu (solid-solutionized) [90]	>100	FCC1	FCC2	1073–1173	10^{-2}–1	1769	-	-	2
CrFeCoNi$Cu_{1.2}$ [66]	>100	FCC1	FCC2	973–1123	10^{-3}–1	1753	9.4–25	394.9 ($\varepsilon_{0.3}$)	2
$Cr_{25}Fe_{15}Co_{45}Ni_{15-}$0.1C [61]	>100	FCC	-	1123–1273	10^{-3}–10^{-1}	1828	4.8–7.8	479.6 ($\varepsilon_{0.5}$)	2
$Cr_{25}Fe_{15}Co_{45}Ni_{15-}$0.05N [61]	>100	FCC	-	1123–1273	10^{-3}–10^{-1}	1828	4.7–6.2	308.5 ($\varepsilon_{0.5}$)	2
$Cr_{10}Mn_{40}Fe_{40}Co_{10-}$3.3 at.%C [29]	225	FCC	-	1173–1373	10^{-2}–1	1727	5.1–10	466.2 ($\varepsilon_{0.6}$)	3
MnFeCoNiCu [32]	>100	FCC	-	1123–1323	10^{-3}–10	1637	3.2–12	510.2 ($\varepsilon_{0.7}$)	3
$CrMn_2FeNi_2Cu$ [95]		FCC1	FCC2	873–1273	10^{-3}–10^{-1}	1692	7.2–15.5	363.3 ($\varepsilon_{0.7}$)	3
TiFeCoNiCu [12]	>100	FCC1	FCC2 + BCC + Ti_2(Ni,Co)	1073–1273	10^{-3}–10^{-1}	1721	2.2–4.5	426.4 ($\varepsilon_{0.7}$)	3
AlCrFeCoN$i_{2.1}$ [22]		FCC	BCC	1073–1373	10^{-3}–10	1692	3.3–5.2	295.5 ($\varepsilon_{0.6}$)	3

Table 1. *Cont.*

Composition	Grain Size (μm)	Major Phase	Minor Phase	T Range (K)	$\dot{\varepsilon}$ Range (s^{-1})	T_m (K)	n_1	Q_c (kJ/mol)	Material Group
$AlCrFeCoNi_{2.1}$ [47]		FCC	BCC	1073–1473	10^{-3}–10	1692	3–5.9	332.9 ($\varepsilon_{0.6}$)	3
AlCrFeNiCu [56]	>100	FCC	BCC	1173–1323	10^{-3}–1	1602	3.3–4.3	154.4 ($\varepsilon_{0.6}$)	3
AlFeCoNiCu [41]	>100	FCC	BCC	1173–1373	10^{-1}–10	1520	5.6–7.2	328.3 ($\varepsilon_{0.5}$)	3
$Al_5Ti_3Cr_{15}Mn_{10}(FeNi)_{67}$ [91]	>100	FCC	BCC	1053–1373	10^{-2}–10^{-1}	1769	4.1–5.3	375.5 ($\varepsilon_{0.6}$)	3
$Mn_5Co_{25}Fe_{25}Ni_{25}Ti_{20}$ [52]		FCC	BCC + Ti_2Ni + Ti_2Co	1073–1273	10^{-3}–1	1791	2.8–4	305.2 ($\varepsilon_{0.6}$)	3
TiZrNbMoHf [11]	>100	BCC	-	1073–1473	10^{-3}–10^{-1}	2444	2.9–6.4	431.4 ($\varepsilon_{0.6}$)	3
TiZrNbMoHf [40]	>100	BCC	-	1373–1523	10^{-3}–5×10^{-1}	2444	3.2–5.1	290.7 ($\varepsilon_{0.6}$)	3
$Ti_{29}Zr_{24}Nb_{23}Hf_{24}$ [74]	361	BCC	-	973–1373	10^{-3}–10	2308	4.1–10	234.6 ($\varepsilon_{0.2}$)	3
TiZrNbHfTa [33]	140	BCC	-	1273–1473	10^{-4}–10^{-2}	2523	2.7–3.3	244.4 ($\varepsilon_{0.6}$)	3
AlCrFeNi [93]	>100	BCC(A2)	BCC(B2)	1073–1373	10^{-3}–1	1663	4.1–8.3	370 ($\varepsilon_{0.6}$)	3
VNbMoTa [68]	>100	BCC	-	1173–1373	10^{-3}–10^{-1}	2780	14.5–19.5	454.2 ($\varepsilon_{0.5}$)	3
$AlTiVNb_2$ [79]	>100	BCC(B2)	-	1273–1473	10^{-3}–10^{-1}	2111	4.1–6.7	391.4 ($\varepsilon_{0.6}$)	3
$AlTi_3VZr_{1.5}Nb$ [99]	>100	BCC(B2)	-	1373–1523	10^{-3}–1	1984	2.9–3	210.6 ($\varepsilon_{0.6}$)	3
AlCrFeCoNiCu [8]	>100	BCC	FCC	973–1303	10^{-3}–10^{-1}	1630	2.9–4.4	300.7 ($\varepsilon_{0.7}$)	3
TiVNbMoTa [71]	0.58	BCC	FCC	1373–1573	5×10^{-4}–5×10^{-1}	2612	2.2–3	291.1 ($\varepsilon_{0.3}$)	3

HEAs with a single FCC phase or FCC (major) + BCC (minor) phases [9,13,18,22,23,25,27,29,32,34,37,41,45,47,52,53,56,60–63,72,84,91,92,96,97,100] have been most extensively studied for hot compression tests (Figure 1c). HEAs with a single BCC phase or BCC (major) + FCC (minor) phases have also been popularly studied [8,11,33,40,42,51,68,71,74,79,93,99]. HEAs with FCC1 and FCC2 or FCC+ intermetallic compound (IMC) precipitates have been recently studied [12,20,38,54,64,66,70,89,90,95].

3. Deformation Mechanisms

The raw data (true stress–true strain curves) in the second and third groups of papers, where a series of hot compression tests were systematically carried out over wide temperature and strain rate ranges, were digitally extracted from the published papers using a software. For example, the true stress–true strain curves for $Al_{0.7}CrMnFeCoNi$ HEA [62] at different temperatures and different strain rates are shown in Figure 2a–d.

The hyperbolic sine Garofalo equation has been widely used to describe the steady-state relationship between the flow stress, temperature, and strain rate ($\dot{\varepsilon}$) over a wide range of temperatures and strain rates where power law creep and power law breakdown (PLB) govern plastic flow [4,104], which is expressed as:

$$\dot{\varepsilon} = A \sinh(\alpha\,\sigma)^n \exp\left(-\frac{Q_c}{RT}\right) \tag{1}$$

where A and α are the experimentally determined material constants, n is the stress exponent, and Q_c is the activation energy for plastic flow. The hyperbolic sine function is mathematically reduced to the equation describing power law creep at low stresses (Equation (2)) and to the equation describing power law breakdown (PLB) at high stresses (Equation (3)):

$$\dot{\varepsilon} = A_1\,(\sigma)^{n_1} \exp\left(-\frac{Q_c}{RT}\right) \tag{2}$$

$$\dot{\varepsilon} = A_2\,\exp(\beta\,\sigma) \exp\left(-\frac{Q_c}{RT}\right) \tag{3}$$

where A_1, A_2, and β are the material constants and n_1 is the stress exponent, which is ideally equal to n, but can be different). The constants α in Equation (1), n_1 in Equation (2), and β in Equation (3) can be related by $\beta = \alpha n_1$ [4,104].

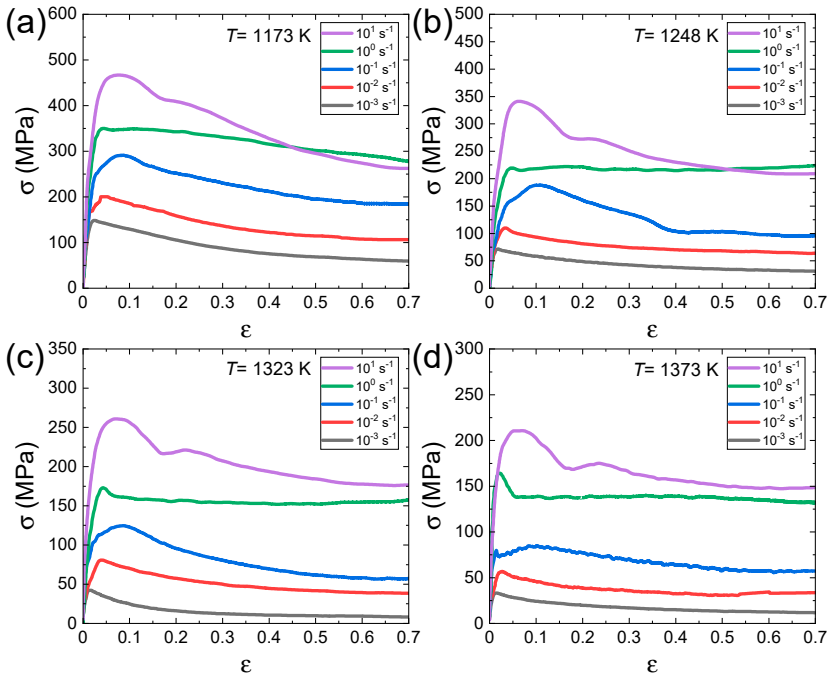

Figure 2. True stress–strain curves for $Al_{0.7}CrMnFeCoNi$ HEA at various strain rates at temperatures of (**a**) 1173, (**b**) 1248, (**c**) 1323, and (**d**) 1373 K. Reproduced/modified with permission from [62], Elsevier.

Figure 3a,b shows the plots of $\log\dot{\varepsilon} - \log\sigma$ and $\log\dot{\varepsilon} - \sigma$ at a given strain of 0.7 for the $Al_{0.7}CrMnFeCoNi$ HEA, where steady-state (SS) flow is attained at almost all temperatures and strain rates. The slopes of the regression lines of the $\log\dot{\varepsilon} - \log\sigma$ and $\log\dot{\varepsilon} - \sigma$ curves are used to determine the values of n_1 and β at each temperature, respectively. Figure 3c shows the plot of $\log\dot{\varepsilon} - \log(\sinh(\alpha\,\sigma))$, where α is the average of the $\alpha(=\beta/n_1)$ values measured at all temperatures. According to Equation (1), the slopes $\left(=\left[\frac{\partial\log\dot{\varepsilon}}{\partial\log(\sinh(\alpha\,\sigma))}\right]_T\right)$ of the $\log\dot{\varepsilon} - \log(\sinh(\alpha\,\sigma))$ curves represent the n value at each temperature. Figure 3d shows the plot of $\log(\sinh(\alpha\,\sigma)) - \frac{1000}{T}$, of which the slope $\left(=\left[\frac{\partial\ln(\sinh(\alpha\,\sigma))}{\partial\left(\frac{1000}{T}\right)}\right]_{\dot{\varepsilon}}\right)$ represents the s value at each strain rate. The Q_c value can be calculated by using the average (N) of the n values measured at different temperatures and the average (S) of the s values measured at different strain rates as follows:

$$Q_c = RNS \tag{4}$$

It is well-known that a value of n_1 represents a specific deformation mechanism; Haper–Dorn creep and diffusional creep are associated with n_1 = 1 [105–108], grain boundary sliding is associated with n_1 = 2 [109,110], solute drag creep is associated with n_1 = 3 [111], dislocation climb creep is associated with 5–7 [112,113], and power law breakdown occurs when $n_1 > 7$ [4]. Jeong and Kim [62] analyzed the tensile, compressive, and creep data of CrMnFeCoNi and $Al_{0.5}CrMnFeCoNi$ HEAs with various grain sizes and proposed the constitutive equations that can quantitatively predict their flow stresses as a function of strain rate, temperature, and grain size (Table 2). Figure 4a,b shows the n_1 values of HEAs with different crystal structures as a function of temperature (T) and a homologous temperature (T/T_m), respectively, where T_m is the melting temperature of the HEAs. As the T_m values of most of the HEAs are not available in the literature, we calculated the

T_m values of the HEAs using the relation $T_m = \sum_{i=1}^{n} c_i (T_m)_i$ [114], where c_i is the atomic percentage of the ith component and $(T_m)_i$ is the melting point of the ith component of the alloy. The plots in Figure 4a,b show that the hot compression tests for the HEAs have been conducted in the temperature range between 873 K and 1573 K, corresponding to the T/T_m range between 0.4 and 0.9. The n_1 value is distributed between 3 and 35, and the n_1 values are most populated between 3 and 7. As T and T/T_m decrease, n_1 tends to increase, and at $T/T_m \leq 0.6$, the number of the data associated with $n_1 \geq 7$ sharply increases. In the T/T_m range between 0.6 and 0.9, the fraction of the data associated with $n_1 \geq 7$ is 0.17, while in the T/T_m range between 0.4 and 0.6, the fraction of $n_1 \geq 7$ is 0.66. This result indicates that PLB dominates plastic flow below 0.6 T/T_m, while power law creep dominates plastic flow above 0.6 T/T_m. It should be noted that the HEAs that show the lowest n_1 of ~3 are the $Al_xCoCrFeNi$ and $Al_xCoCrFeMnNi$ HEAs with BCC or BCC + FCC (minor) phases, containing an Al element. Figure 4c shows that the n values of the HEAs are slightly smaller than their n_1 values. They mostly range between 2.5 and 5. The n tends to increase as T/T_m decreases, but it is not as sensitive as n_1 to T/T_m variation.

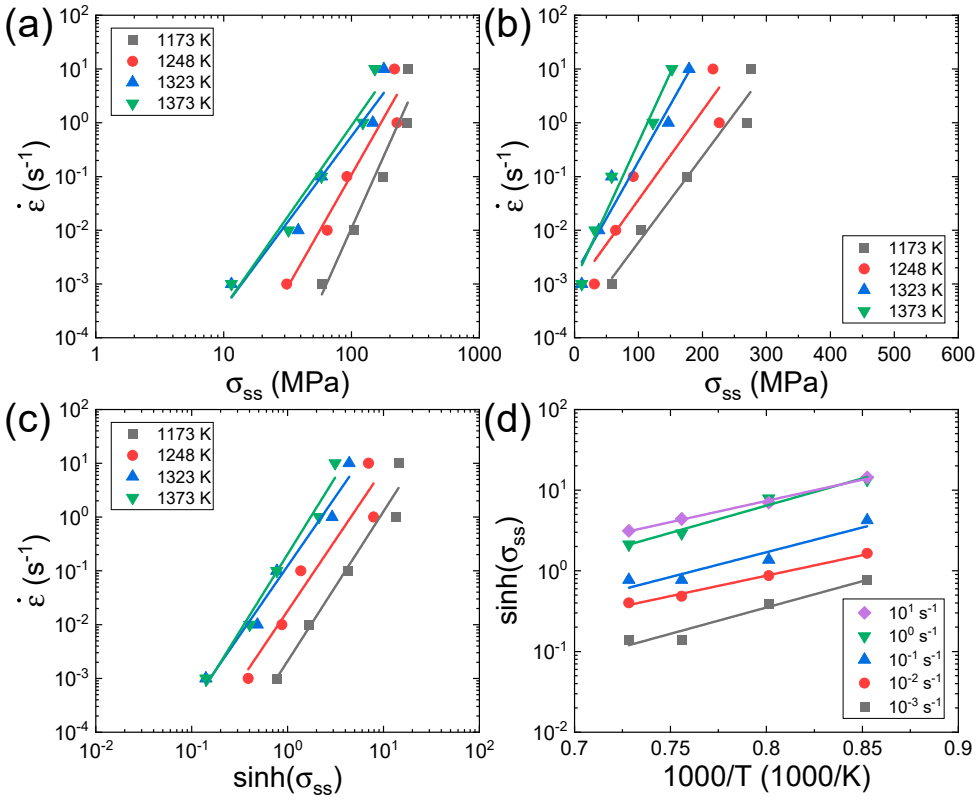

Figure 3. Plots of (**a**) $\log \dot{\varepsilon} - \log \sigma$, (**b**) $\log \dot{\varepsilon} - \sigma$, (**c**) $\log \dot{\varepsilon} - \log(\sinh(\alpha\, \sigma))$, and (**d**) $\log(\sinh(\alpha\, \sigma)) - \frac{1000}{T}$ for the $Al_{0.7}CrMnFeCoNi$ HEA [62] at a given strain of 0.7. The subscript '*ss*' in σ_{ss} represents the steady state. Reproduced/modified with permission from [62], Elsevier.

Table 2. The constitutive equations of deformation mechanisms in HEAs.

Creep Process	Equation	k_i Value		
		Ruano et al. [113]	CrMnFeCoNi [62]	$Al_{0.5}CrMnFeCoNi$ [62]
Diffusional creep				
Nabarro–Herring [105,106]	$\dot{\varepsilon}_1 = k_1(D_L/d^2)(Eb^3/kT)(\sigma/E)$	14	14	14
Coble [107]	$\dot{\varepsilon}_2 = k_2(D_{gb}b/d^3)(Eb^3/kT)(\sigma/E)$	50	50	50
Grain boundary sliding (GBS)				
Lattice-diffusion-controlled [109]	$\dot{\varepsilon}_3 = k_3(D_L/d^2)(\sigma/E)^2$	6.4×10^9	3.1×10^8	6.7×10^8
Pipe-diffusion-controlled [110]	$\dot{\varepsilon}_4 = k_4\alpha(D_p/d^2)(\sigma/E)^4$	3.2×10^{11}	1.6×10^{10}	3.4×10^{10}
Grain-boundary-diffusion-controlled [109]	$\dot{\varepsilon}_5 = k_5(D_{gb}b/d^3)(\sigma/E)^2$	5.6×10^8	1.9×10^7	5.9×10^7
Slip creep				
Harper–Dorn [108]	$\dot{\varepsilon}_6 = k_6(D_L/b^2)(Eb^3/kT)(\sigma/E)$	1.7×10^{-11}	1.7×10^{-11}	1.7×10^{-11}
Lattice-diffusion-controlled dislocation climb creep [112]	$\dot{\varepsilon}_7 = k_7(D_L/b^2)(\sigma/E)^5$	1×10^{11}	2.6×10^9	1.5×10^9
Pipe-diffusion-controlled dislocation climb creep [112]	$\dot{\varepsilon}_8 = k_8(D_p/b^2)(\sigma/E)^7$	5×10^{12}	1.1×10^9	3.9×10^9
Solute drag creep [111]	$\dot{\varepsilon}_{CJ} = \frac{2\gamma\tilde{D}kT}{X_s X_a e^2 E b^5}[2(1+\nu)]^4\left(\frac{1-\nu}{1+\nu}\right)\left(\frac{\sigma}{E}\right)^3$			

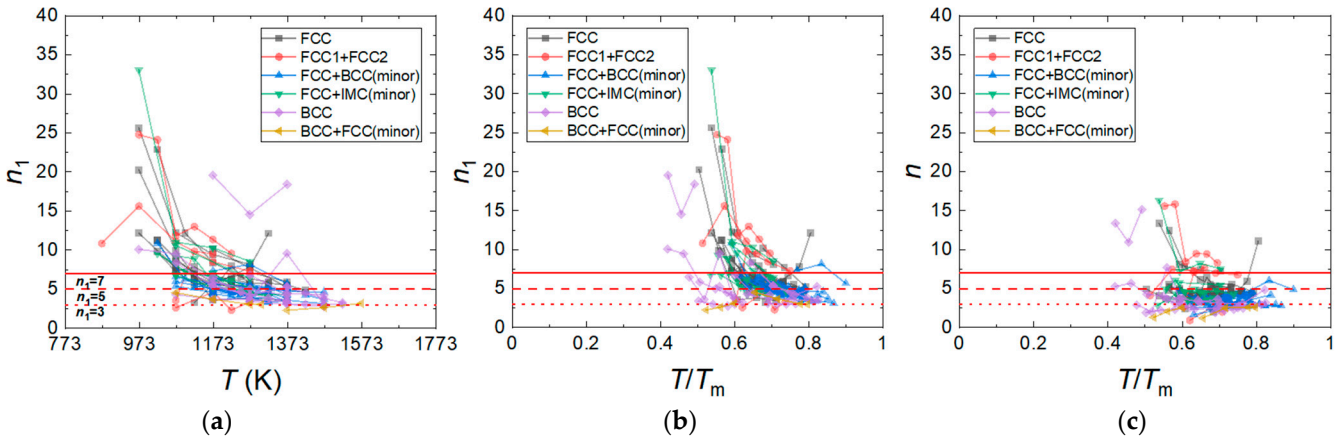

Figure 4. n_1 values of the HEAs with different crystal structures as a function of (**a**) temperature (T) and (**b**) homologous temperature (T/T_m). (**c**) n values of the HEAs as a function of T/T_m.

Figure 5a,b shows the $\log\dot{\varepsilon} - \log\sigma$ curves for the $Al_xCrMnFeCoNi$ (x = 0–1) [9,27,34,42,63] and $Al_xCrFeCoNi$ (x = 0–1) HEAs [13,25,51,53,72,84,92,96] at a given temperature of 1173 K. The n_1 value decreases from 5 to ~3 as x increases. This result indicates that as the amount of BCC phase (rich with Al) increases, the characteristics of viscous glide creep associated with n_1~3 become more pronounced. Jeong and Kim [42] analyzed the deformation behavior of the AlCrMnFeCoNi HEA and found that aluminum, which is largest in size among the constituent elements [42], acts as a solute that causes solute drag creep and showed that the solute drag creep model proposed by Hong and Weertman [111] for conventional metals can quantitatively explain the deformation behavior of the AlCrMnFeCoNi HEA with reasonable assumptions on the diffusivity of Al in the HEA. From the plots in Figure 5a,b, it should also be noted that flow stress tends to decrease the added amount of Al increases especially at low strain rates, indicating that the BCC phase deforming under solute drag creep is weaker than the FCC phase deforming under dislocation climb creep.

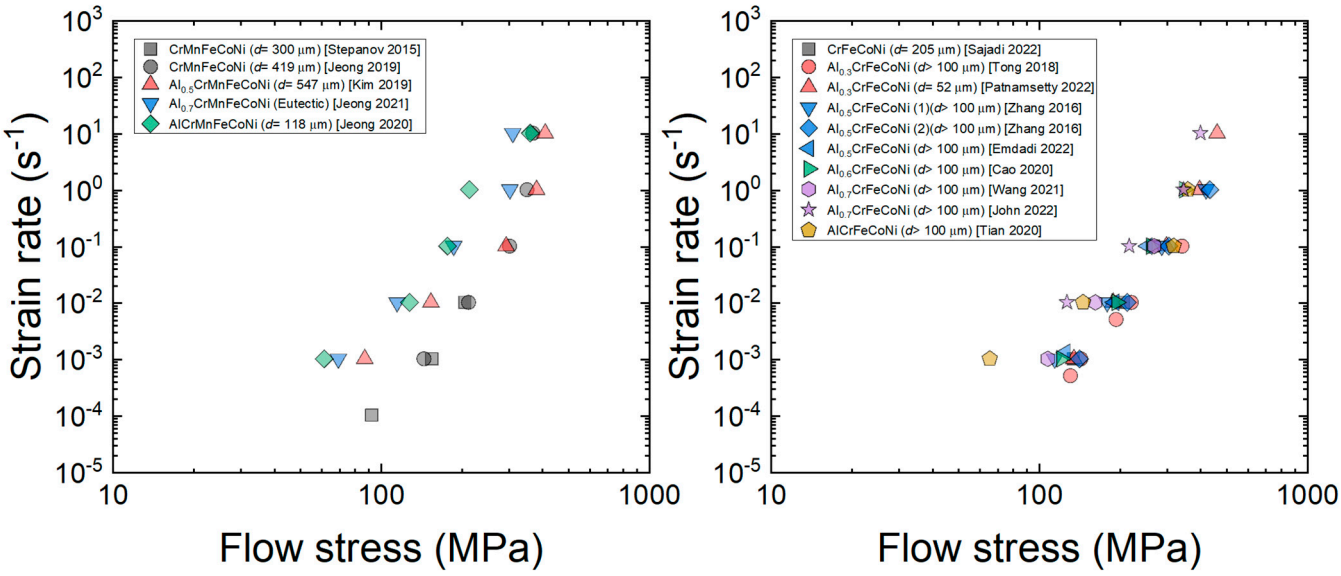

(**a**) (**b**)

Figure 5. Plots of the $\log\dot{\varepsilon} - \log\sigma$ curves for the (**a**) $Al_xCrMnFeCoNi$ (x = 0–1) [9,27,34,42,63] and (**b**) $Al_xCrFeCoNi$ (x = 0–1) [13,25,51,53,72,84,92,96] HEAs at a given temperature of 1173 K (at a strain of 0.5).

Deformation mechanism maps represent the dominant deformation mechanism for a given metallic material under different conditions. Figure 6a,b shows the deformation mechanism maps as a function of strain rate (10^{-5} to 10 s^{-1}) and temperature (873 and 1573 K) at a given (coarse) grain size of 100 μm for CoCrFeMnNi and $Al_{0.5}$CoCrFeMnNi. On the maps, the data of the CoCrFeMnNi and $Al_{0.5}$CoCrFeMnNi HEAs are loaded. For the CoCrFeMnNi HEA, at high temperatures, dislocation climb creep controlled by lattice diffusivity (D_L) governs plastic flow, but when the temperature is low, the rate-controlling mechanism changes to dislocation climb creep controlled by D_p (or PLB). As the strain rate increases, the region associated with D_p-controlled dislocation climb creep (or PLB) expands to a higher temperature. For the $Al_{0.5}$CoCrFeMnNi, solute drag creep appears in the bottom right corner of the map. Jeong and Kim [62] showed that when the grain size is sufficiently small, grain boundary sliding mechanism can play a more important role than solute drag creep in the $Al_{0.5}$CoCrFeMnNi HEA.

Figure 7a shows the Q_c values of HEAs calculated using Equation (4). The Q_c value is in the range between 150 and 600 kJ/mol, and the data distribution is most populated in the range between 300 and 400 kJ/mol. The activation energy of the tracer diffusivity of elements in the HEAs ranges between 240 and 408 kJ/mol [115,116], implying that the activation energy of plastic flow for the HEA is related to the atomic diffusivity of elements constituting the HEAs. Figure 7b shows the relation between n_1 and Q_c for the HEAs. A smaller Q_c is obtained at smaller n_1, and this is more apparent near n_1~3, where solute drag creep governs the deformation mechanism. It is worthwhile to note that the activation energy for the solute diffusion (Q_{solute}) of magnesium in aluminum (136 kJ mol^{-1}) is lower than the activation energy for self-diffusion in pure aluminum (142 kJ/mol) [117].

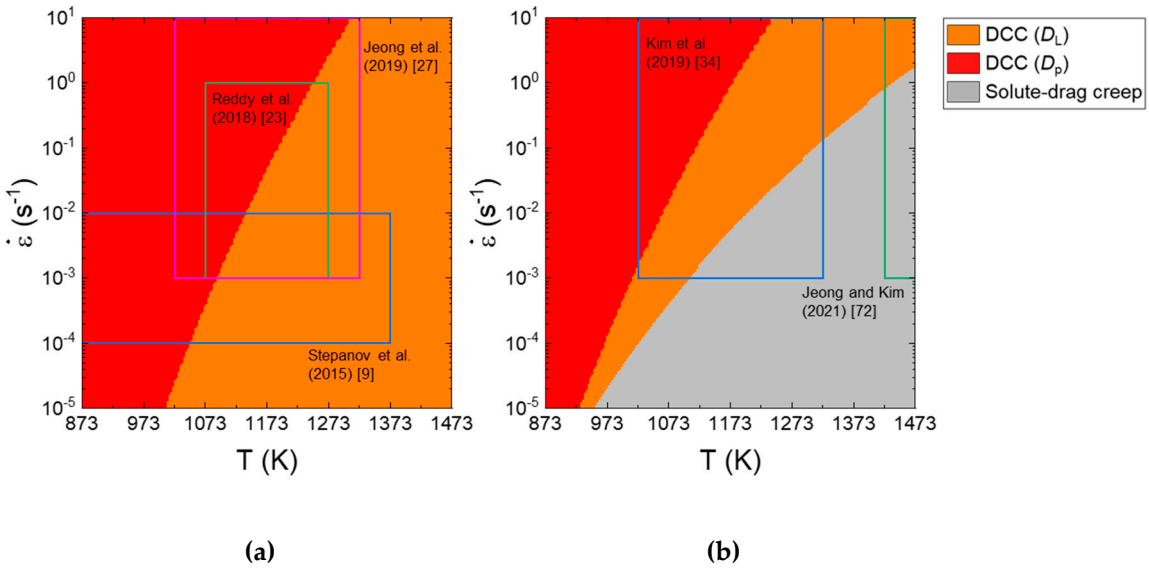

(a) **(b)**

Figure 6. Deformation mechanism maps as a function of strain rate and temperature at a given grain size of 100 μm for (**a**) CoCrFeMnNi and (**b**) $Al_{0.5}CoCrFeMnNi$. Reproduced/modified with permission from [62], Elsevier.

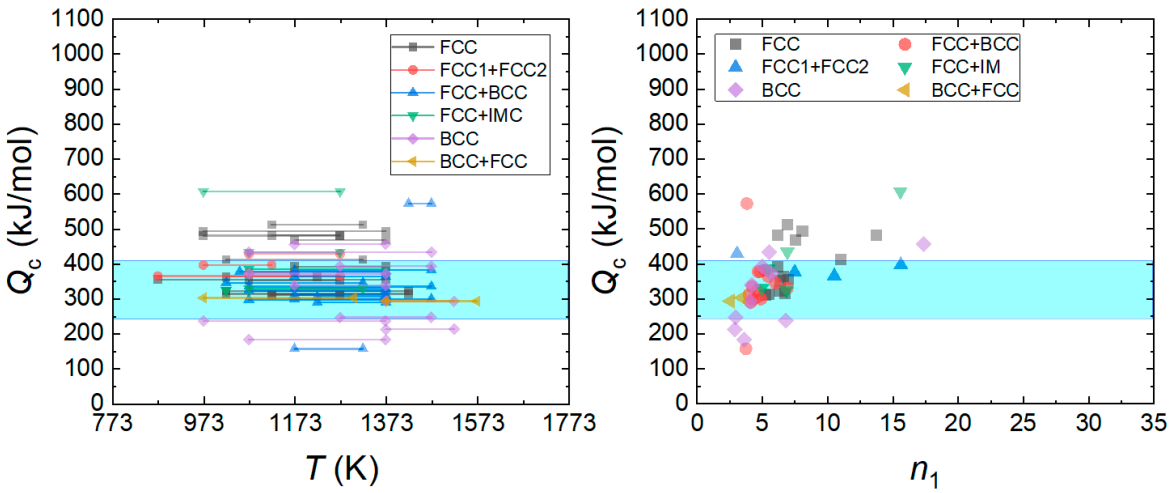

(a) **(b)**

Figure 7. (**a**) Q_c values of HEAs calculated using Equation (4) and (**b**) the relation between n_1 and Q_c for the HEAs. The activation energy (Q_L^*) of tracer diffusivity of elements in the $Al_xCoCrFeMnNi$ and $Al_xCoCrFeNi$ HEAs ranges between 240 and 408 kJ/mol (shaded area by blue color): Q_L^* = 323 ± 5 kJ/mol for Cr, Q_L^* = 303 ± 3 kJ/mol for Fe, Q_L^* = 240 ± 20 kJ/mol for Co, Q_L^* = 253 ± 8 kJ/mol for Ni in CrFeCoNi, Q_L^* = 313 ± 13 kJ/mol for Cr, Q_L^* = 272 ± 13 kJ/mol for Mn, Q_L^* = 309 ± 11 kJ/mol for Fe, Q_L^* = 270 ± 22 kJ/mol for Co, and Q_L^* = 304 ± 9 kJ/mol for Ni in CrMnFeCoNi [115]. Q_L^* = 263 kJ/mol for Al, Q_L^* = 288 kJ/mol for Cr, Q_L^* = 315 kJ/mol for Fe, Q_L^* = 258 kJ/mol for Co, Q_L^* = 260 kJ/mol for Ni in $Al_{4.88}Co_{29.53}Cr_{18.58}Fe_{19.62}Ni_{27.39}$ [117], Q_L^* = 258 kJ/mol for Al, Q_L^* = 288 kJ/mol for Cr, Q_L^* = 408 kJ/mol for Fe, Q_L^* = 260 kJ/mol for Co, and Q_L^* = 261 kJ/mol for Ni $Al_{6.64}Co_{23.82}Cr_{23.66}Fe_{23.01}Ni_{22.87}$ [116].

4. Processing Maps

A processing map, which is useful in finding the optimal condition for hot forging or extrusion, is composed of a power dissipation map and a flow instability map. According to Prasad et al. [101], the total power, P, absorbed in a material is divided into the power dissipation content (G), which represents the power dissipated by plastic deformation

giving rise to a temperature increase in the workpiece and the power dissipation co-content (J), which represents the power dissipated by a change in its microstructure, such as dynamic recovery and dynamic recrystallization [101].

$$P = \sigma\dot{\varepsilon} = G + J = \int_0^{\dot{\varepsilon}} \sigma d\dot{\varepsilon} + \int_0^{\sigma} \dot{\varepsilon} d\sigma \tag{5}$$

The efficiency of power dissipation, η, which represents the power dissipation efficiency due to a change in microstructure during plastic flow, is defined as [101]:

$$\eta = \frac{J}{J_{max}} = 2\left(1 - \frac{1}{\sigma\dot{\varepsilon}} \int_0^{\dot{\varepsilon}} \sigma d\dot{\varepsilon}\right) \tag{6}$$

where J_{max} is the maximum J value (=$P/2$).

The strain rate sensitivity, m, which is equal to $1/n_1$, can be calculated by:

$$m = \frac{1}{n_1} = \left[\frac{\partial ln\sigma}{\partial ln\dot{\varepsilon}}\right] \tag{7}$$

When m is assumed to be constant over the investigated strain rate range (as assumed by Prasad et al. [101]), $\eta = \frac{2m}{m+1}$, but when m is not constant (as considered by Murty et al. [118]), η can be directly determined from Equation (6) by calculating $\int_0^{\dot{\varepsilon}} \sigma d\dot{\varepsilon}$ through the numerical integration procedure, using Equation (8):

$$\int_0^{\dot{\varepsilon}} \sigma d\dot{\varepsilon} = \int_0^{\dot{\varepsilon}_{min}} \sigma d\dot{\varepsilon} + \int_{\dot{\varepsilon}_{min}}^{\dot{\varepsilon}} \sigma d\dot{\varepsilon} = \left(\frac{\sigma\dot{\varepsilon}}{m+1}\right)_{\dot{\varepsilon}_{min}} + \int_{\dot{\varepsilon}_{min}}^{\dot{\varepsilon}} \sigma d\dot{\varepsilon} \tag{8}$$

In drawing the flow instability map, Ziegler's plastic flow theory is used, and according to Murty et al. [119] (when m is not a constant),

$$\xi = 2m - \eta < 0 \tag{9}$$

When ξ is negative, deformation in the material is predicted to be unstable, such that localized flow, adiabatic shear banding, or cracking can take place.

Kim and Jeong [120] suggested an empirical equation for η by analyzing the behavior of η values of many metals calculated by following the numerical method proposed by Murty (Equation (8)) as a function of n_1:

$$\eta = \left[\frac{10^4}{(n_1-1)^2}\right]\left(\frac{2}{n_1+1}\right) + \left[\frac{\tanh(n_1-5)+1}{2} \cdot \frac{(n_1-1)^{1.5}}{(n_1-1)^{1.5}+10^2}\right]\left(\frac{2}{n_1} \cdot \frac{e^{n_1}-1}{e^{n_1}}\right) \tag{10}$$

By using this equation, the η value can be easily obtained once n_1 is known without numerically solving Equation (8). Kim and Jeong [121] also presented a simple form of the flow instability criterion based on the observation that unstable flow occurs in many metals when n_1 is larger than 7 (i.e. when PLB governs plastic flow):

$$\xi = 7 - n_1 < 0 \text{ or } \eta < 0.285 \tag{11}$$

Unlike in the procedure for determining n_1 for calculating Q_c (Figure 3a), where a linear fitting is applied to the data in the plot of $\log\dot{\varepsilon} - \log\sigma$, the n_1 value as a function of strain rate, temperature, and strain, which is necessary for constructing processing maps, has often been determined using a third- or fourth-order polynomial fitting to the data in the plot of $\log\dot{\varepsilon} - \log\sigma$. This polynomial fitting curve, however, sometimes has difficulty describing the power law creep. This example is shown in Figure 8. Thus, Kim

and Jeong [121] proposed the exponential fitting method for the determination of the m from the plot of $\log\dot{\varepsilon} - \log\sigma$. According to the method,

$$\log\dot{\varepsilon} = \mathrm{a} + \mathrm{c} \times \exp\left(\frac{\log\sigma - b}{d}\right) + f \times \exp\left(\frac{\log\sigma - b}{g}\right) \tag{12}$$

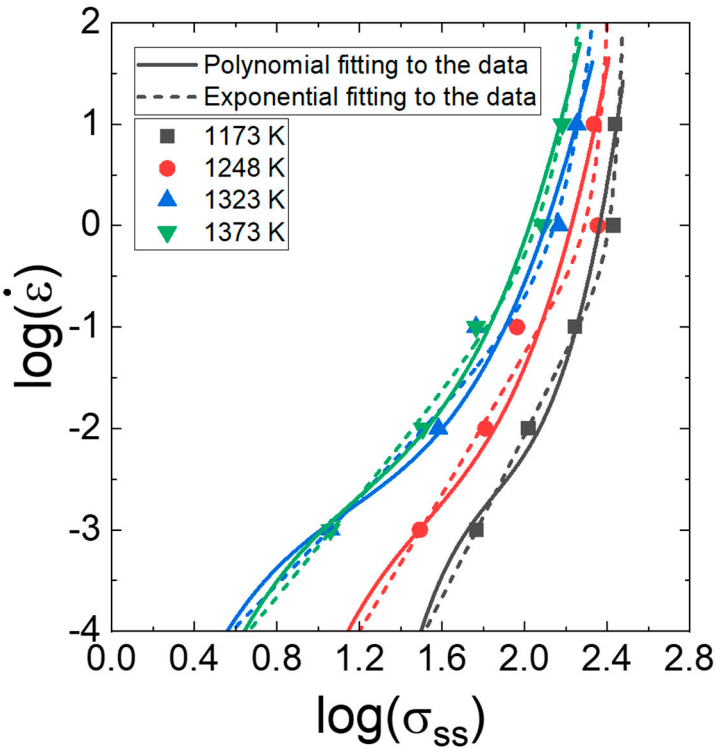

Figure 8. Polynomial fitting and exponential fitting to the data points in the plot in Figure 3a. Reproduced/modified with permission from [63], Elsevier.

When Equation (12) is used, m can be calculated by Equation (13):

$$m = \left[\frac{c}{d} \times \exp\left(\frac{\log\sigma - b}{d}\right) + \frac{f}{g} \times \exp\left(\frac{\log\sigma - b}{g}\right)\right]^{-1} \tag{13}$$

As observed in Figure 8, the exponential fitting, where m tends to decrease gradually with increasing strain rate, provides a better fit to the series of data compared with the polynomial fitting, which sometimes creates uncertain fluctuation between the data points.

Figure 9a–c shows the η values of the HEAs calculated by Murty's method (Equations (6) and (8)) as a function of n_1 for the three material groups of HEAs. It is obvious that the η values of all the three material groups of HEAs follow Equation (10) well in the entire range of n_1, regardless of the differences in composition and crystal structure. Furthermore, it is observed that the flow instability condition determined by Equation (9) occurs at $n_1 \approx 7$, supporting that the onset of flow instability occurs at the transition from power law creep to PLB (Equation (11)).

Figure 10a–d shows the processing maps for $Al_{0.5}CrMnFeCoNi$ and $Al_{0.3}CrFeCoNi$ HEAs constructed based on Murty's approach and Kim and Jeong's approach. A good match is observed between the two methods in power dissipation maps as well as flow instability maps. However, some mismatch is observed for the $Al_{0.3}CrFeCoNi$ HEA in the flow instability at low strain rates and at low temperatures. This occurs because in Murty's method, the material is assumed to follow the power law creep at low strain rates below $\dot{\varepsilon}_{min}$ (Equation (8)), but this assumption can be wrong at low temperatures if PLB governs plastic flow below $\dot{\varepsilon}_{min}$.

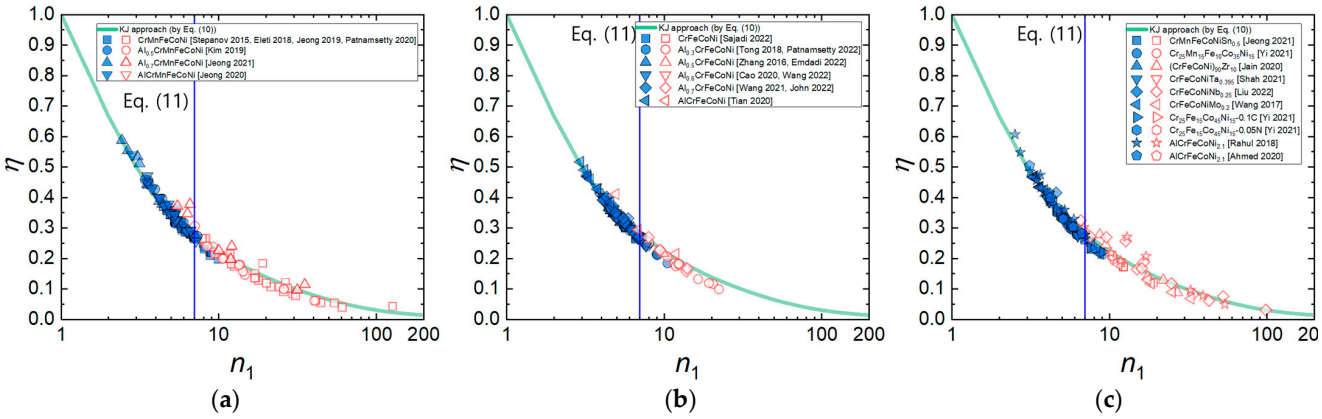

Figure 9. η values of the HEAs calculated by Murty's method as a function of n_1 for (**a**) $Al_xCrMnFeCoNi$ (x = 0–1) [9,23,27,34,42,45,63], (**b**) $Al_xCrFeCoNi$ (x = 0–1) [13,25,51,53,72,84,92,96,97,100], and (**c**) $CrMnFeCoNiSn_{0.5}$, etc. [18,22,47,54,60,61,64,70,89], which can be fitted by Equation (10). The (blue) solid and (red) open symbols represent the data points belonging to the flow stability and flow instability regimes, respectively, which is determined by Equation (9).

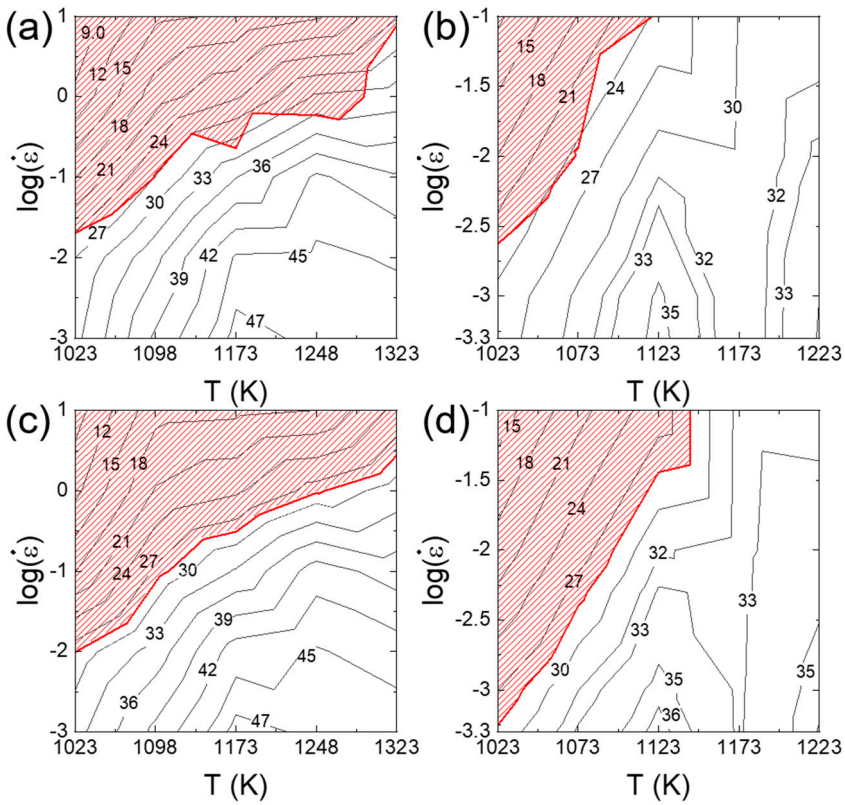

Figure 10. 2D processing maps for (**a**,**c**) $Al_{0.5}CrMnFeCoNi$ and (**b**,**d**) $Al_{0.3}CrFeCoNi$ constructed based on Murty's approach and Kim and Jeong's approach using the raw data from [62] (for $Al_{0.5}CrMnFeCoNi$) and [92] (for $Al_{0.3}CrFeCoNi$).

Figure 11a,b shows the plots of n_1 as a function of the Zener–Hollomon parameter ($Z = \exp(\frac{Q_c}{RT})$) for $Al_{0.5}CrMnFeCoNi$ and $Al_{0.3}CrFeCoNi$. There is a good correlation between n_1 and Z, indicating that as strain rate increases and temperature decreases (i.e., as Z increases), n_1 tends to increase. This occurs because according to the deformation mechanism maps (Figure 6a,b), as strain rate increases and temperature decreases, the deformation mechanism changes from solute drag creep (associated with n_1 = 3) to disloca-

tion climb creep (associated with n_1 = 5) and then power law breakdown (associated with n_1 > 3). η is a function of n_1 according to Equation (10). Hence, η can also be expressed as a function of Z. Figure 11c,d shows the plot of η as a function of Z for $Al_{0.5}CrMnFeCoNi$ and $Al_{0.3}CrFeCoNi$, where a good correlation between η and Z is observed. η tends to decrease as Z increases. In addition, most of the data belonging to the flow instability condition (determined by Murty's approach using Equation (9)) are positioned below $\eta = 0.285$, supporting the validity of Equation (11). Some mismatches are observed between Equation (9) and Equation (10) and this can be attributed to the aforementioned assumption of power law creep below $\dot{\varepsilon}_{min}$ in Murty's method.

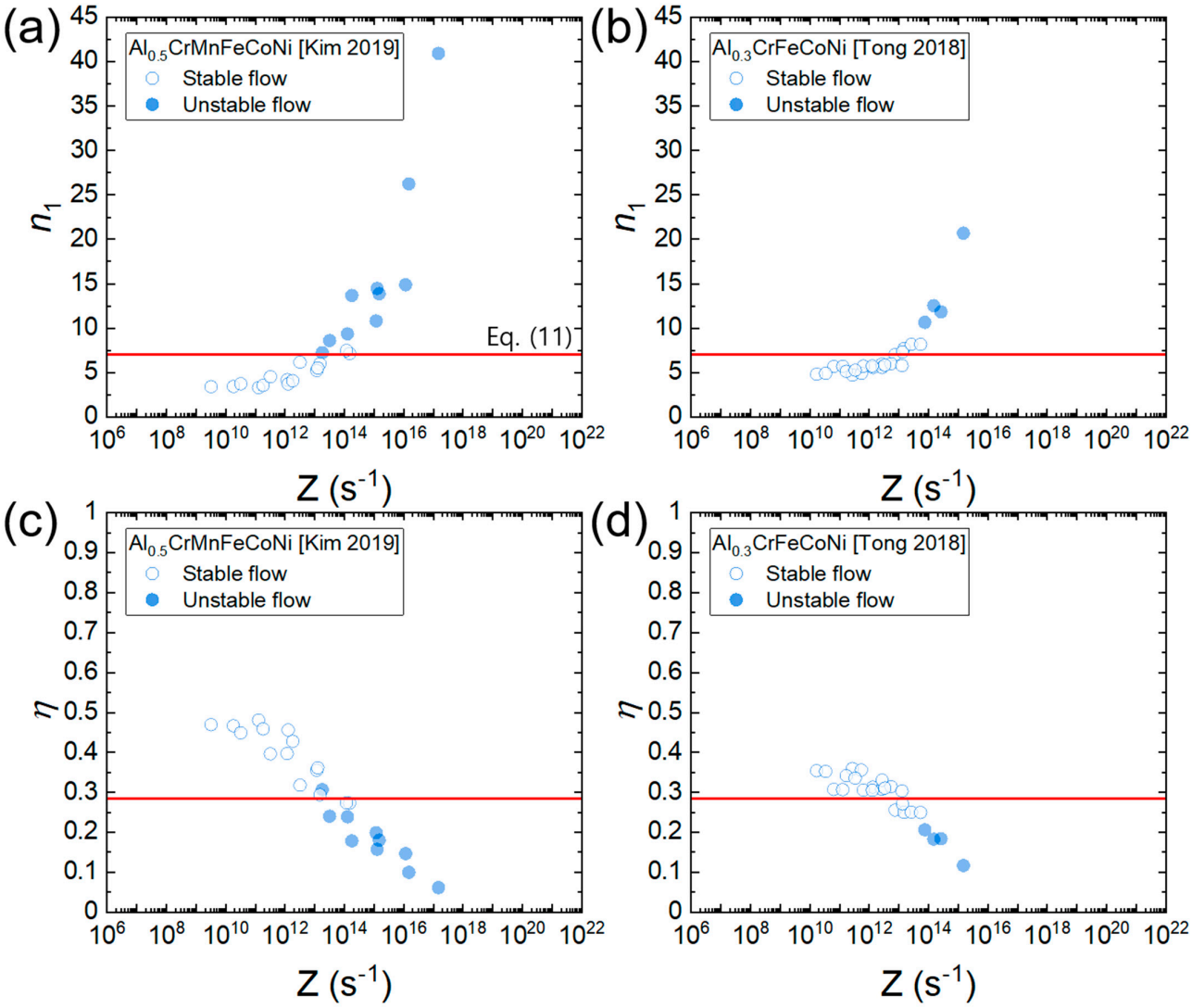

Figure 11. Plot of n_1 and η as a function of Z for (**a**,**c**) $Al_{0.5}CrMnFeCoNi$ [34] and (**b**,**d**) $Al_{0.3}CrFeCoNi$ [25]. Open and solid symbols represent the flow stability and instability conditions (determined by Equation (9)), respectively. A red horizontal line represents $\eta = 0.285$ (Equation (11)).

The plots in Figure 11c,d represent the "processing maps expressed as a function of Z" because if one knows the temperature and strain rate, the Z value can be calculated, and then the power dissipation efficiency and flow (in)stability can be readily determined from the plot.

Figure 12a–c shows the plots of processing maps for the three material groups of HEAs expressed as a function of Z using each Q_c value of the HEAs (Table 1), and Figure 12d shows the plot where all the data in Figure 12a–c overlap. The η values of each material are well correlated as a function of Z, and the data for each group converge to a

common curve. Also, it is observed that all the data of the three groups converge to a single common curve. According to the plot in Figure 12d, flow stability is nearly guaranteed at $Z \leq 10^{12}$ s^{-1}, while flow instability is nearly inevitable at $Z \geq 2 \times 10^{15}$ s^{-1}. At 10^{12} s^{-1} $\leq Z \leq 2 \times 10^{15}$ s^{-1}, flow stability and instability conditions coexist, and flow instability becomes more dominant as Z increases.

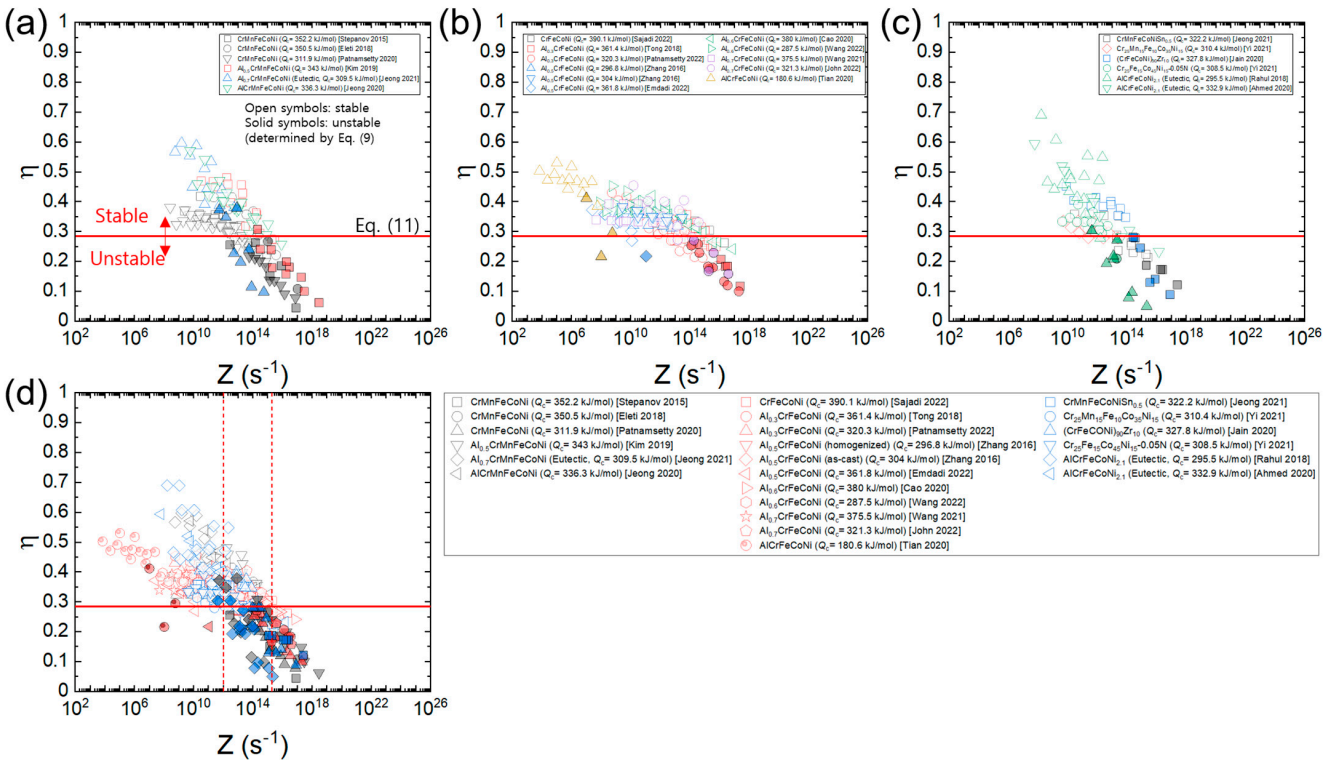

Figure 12. Plots of processing maps for (**a**) $Al_xCrMnFeCoNi$ (x = 0–1) [9,23,34,42,45,63], (**b**) $Al_xCrFeCoNi$ (x = 0–1) [13,25,51,53,72,84,92,96,97,100], and (**c**) $CrMnFeCoNiSn_{0.5}$, etc. [22,47,54,60,61,64], expressed as a function of Z using each Q_c value of the HEAs (Table 1) and (**d**) the plot where all the data in (**a**–**c**) overlap. Open and solid symbols represent the flow stability and instability conditions (determined by Equation (9)), respectively. A red horizontal line represents $\eta = 0.285$ (Equation (11)).

Figure 13a–c shows the plots of processing maps for the three material groups of HEAs constructed as a function of Z using the average Q_c value of all the HEAs (317.2 kJ/mol), and Figure 12d shows the plot where all the data in Figure 13a–c overlap. Note that all the data lie close to a common curve. According to the plot in Figure 12d, flow stability prevails at $Z \leq 10^{12}$ s^{-1}, while flow instability prevails at $Z \geq 3 \times 10^{14}$ s^{-1}. By plotting in this fashion, one can easily compare the η values of the different HEAs at a given temperature and strain rate as well as predict the optimum hot working conditions of the HEAs with unknown Q_c values.

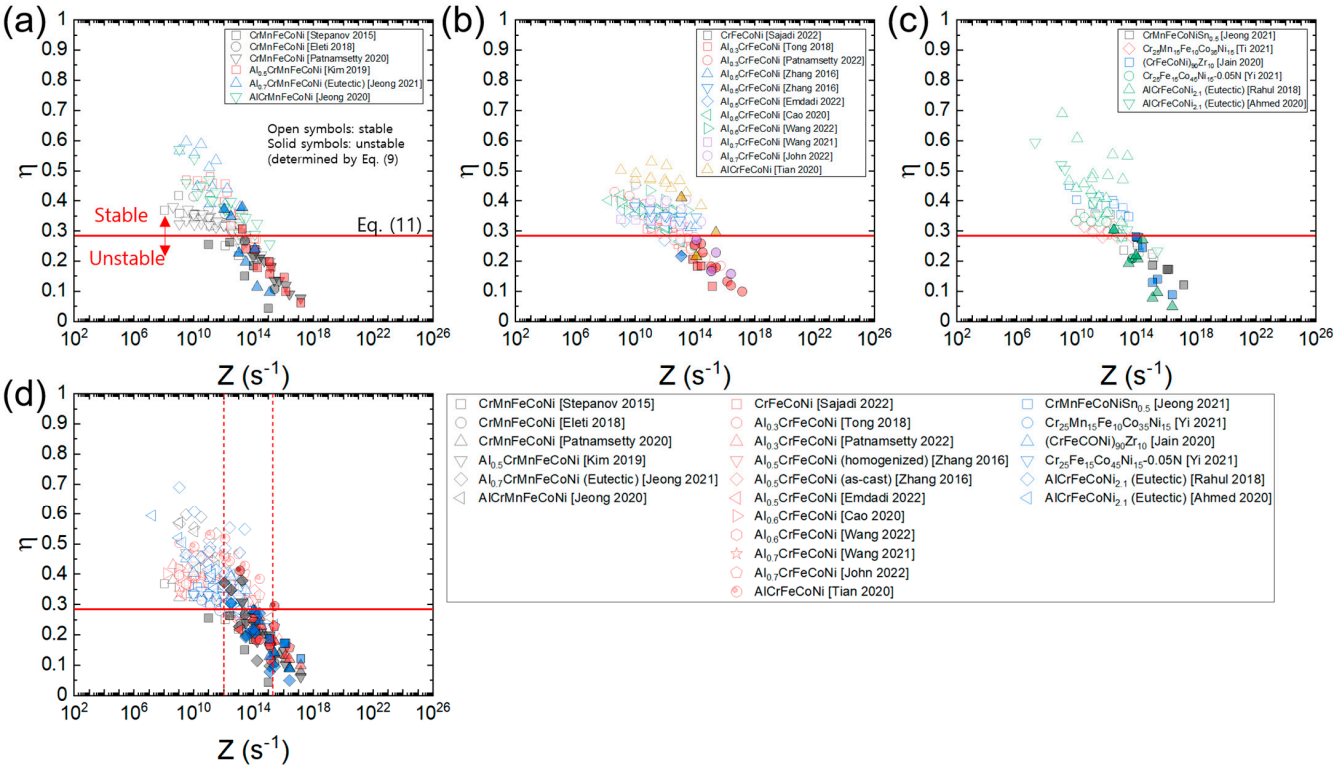

Figure 13. Plots of processing maps for (**a**) $Al_xCrMnFeCoNi$ (x = 0–1) [9,23,34,42,45,63], (**b**) AlxCrFeCoNi (x = 0–1) [13,25,51,53,72,84,92,96,97,100], and (**c**) CrMnFeCoNiSn0.5, etc. [22,47,54,60,61,64], expressed as a function of Z using the average Qc value of all the HEAs (317.2 kJ/mol) and (**d**) the plot where all the data in (**a**–**c**) overlap. Open and solid symbols represent the flow stability and instability conditions (determined by Equation (9)), respectively. A red horizontal line represents $\eta = 0.285$ (Equation (11)).

5. Conclusions

The hot compressive behaviors of the HEA materials with different chemical compositions and crystal structures and processing maps were analyzed, and the following observations were made.

1. Hot compression tests on many HEAs have been conducted in the temperature range between 873 K and 1573 K, corresponding to the T/T_m range between 0.4 and 0.9. The n_1 values are most populated between 3 and 7.
2. As T/T_m decreases, n_1 tends to increase, and power law breakdown typically occurs at $T/T_m \leq 0.6$.
3. In $Al_xCrMnFeCoNi$ (x = 0–1) and $Al_xCrFeCoNi$ (x = 0–1) HEAs, n_1 tends to increase as the concentration of Al increases, implying that Al acts as a solute atom that exerts a drag force on dislocation slip motion.
4. The activation energy for plastic flow (Q_c) in the HEAs is calculated to be in the range between 150 and 600 kJ/mol, and the data distribution is populated in the Q_c value range between 300 and 400 kJ/mol. The average Q_c value for all the HEAs is 317 kJ/mol.
5. The η value of the HEAs can be expressed as a function of n_1 only. Flow instability is shown to occur near n_1 = 7, implying that the onset of flow instability occurs at the transition from power law creep to PLB.
6. Processing maps for all the HEAs are demonstrated to be constructed using the Zener–Hollomon parameter ($Z = \exp\left(\frac{Q_c}{RT}\right)$). According to the analysis result, flow stability prevails at $Z \leq 10^{12}$ s^{-1} in all HEAs.

Author Contributions: Conceptualization, W.J.K.; formal analysis, H.T.J.; writing—original draft preparation, H.T.J.; writing—review and editing, W.J.K.; supervision, W.J.K. All authors have read and agreed to the published version of the manuscript.

Funding: This research was financially supported by the Mid-Career Researcher Program through the National Research Foundation of Korea funded by the Ministry of Education, Science and Technology (NRF-2020R1A2C1008105).

Data Availability Statement: The raw/processed data required to reproduce these findings cannot be shared at this time, as the data also form part of an ongoing study.

Conflicts of Interest: The authors declare no conflict of interest.

References

1. George, E.P.; Raabe, D.; Ritchie, R.Q. High-entropy alloys. *Nat. Rev. Mater.* **2019**, *4*, 515–534. [CrossRef]
2. Tsai, M.H.; Yeh, J.W. High-entropy alloys: A critical review. *Mater. Res. Lett.* **2014**, *2*, 107–123. [CrossRef]
3. Li, W.; Xie, D.; Li, D.; Zhang, Y.; Gao, Y.; Liaw, P.K. Mechanical behavior of high-entropy alloys. *Prog. Mater. Sci.* **2021**, *118*, 100777. [CrossRef]
4. Sherby, O.D.; Burke, P.M. Mechanical behavior of crystalline solids at elevated temperature. *Prog. Mater. Sci.* **1968**, *13*, 323–390. [CrossRef]
5. Sherby, O.D.; Wadsworth, J. Superplasticity-Recent advances and future directions. *Prog. Mater. Sci.* **1989**, *33*, 169–221. [CrossRef]
6. Senkov, O.D.; Wilks, G.B.; Scott, J.M.; Miracle, D.B. Mechanical properties of $Nb_{25}Mo_{25}Ta_{25}W_{25}$ and $V_{20}Nb_{20}Mo_{20}Ta_{20}W_{20}$ refractory high entropy alloys. *Intermetallics* **2011**, *19*, 698–706. [CrossRef]
7. Senkov, O.D.; Scott, J.M.; Senkova, S.V.; Meisenkothen, F.; Miracle, D.B.; Woodward, C.F. Microstructure and elevated temperature properties of a refractory TaNbHfZrTi alloy. *J. Mater. Sci.* **2012**, *47*, 4062–4074. [CrossRef]
8. Nayan, N.; Singh, G.; Murty, S.V.S.N.; Jha, A.K.; Pant, B.; George, K.M.; Ramamurty, U. Hot deformation behaviour and microstructure control in AlCrCuNiFeCo high entropy alloy. *Intermetallics* **2014**, *55*, 145–153. [CrossRef]
9. Stepanov, N.D.; Shaysultanov, D.G.; Yurchenko, N.; Zherebtsov, S.V.; Ladygin, A.N.; Salishchev, G.A.; Tikhonovsky, M.A. High temperature deformation behavior and dynamic recrystallization in CoCrFeNiMn high entropy alloy. *Mater. Sci. Eng. A* **2015**, *636*, 188–195. [CrossRef]
10. Chen, H.; Kauffmann, A.; Gorr, B.; Schliephake, D.; Seemüller, C.; Wagner, J.; Christ, H.; Heilmaier, M. Microstructure and mechanical properties at elevated temperatures of a new Al-containing refractory high-entroy alloy Nb-Mo-Cr-Ti-Al. *J. Alloys Compd.* **2016**, *661*, 206–215. [CrossRef]
11. Guo, N.; Wang, L.; Luo, L.; Li, X.; Chen, R.; Su, Y.; Guo, J.; Fu, H. Hot deformation characteristics and dynamic recrystallization of the MoNbHfZrTi refractory high-entropy alloy. *Mater. Sci. Eng. A* **2016**, *651*, 698–707. [CrossRef]
12. Samal, S.; Rahul, M.; Kottada, R.; Phanikumar, G. Hot deformation behaviour and processing map of Co-Cu-Fe-Ni-Ti eutectic high entropy alloy. *Mater. Sci. Eng. A* **2016**, *664*, 227–235. [CrossRef]
13. Zhang, Y.; Li, J.; Wang, J.; Niu, S.; Kou, H. Hot deformation behavior of as-cast and homogenized $Al_{0.5}CoCrFeNi$ high entropy alloys. *Metals* **2016**, *6*, 277. [CrossRef]
14. Lee, K.; Bae, B.; Kang, J.; Kim, K.; Na, Y. Multi-phase refining of an AlCoCrFeNi high entropy alloy by hot compression. *Mater. Lett.* **2017**, *198*, 81–84. [CrossRef]
15. Xian, X.; Zhong, Z.; Zhang, B.; Song, K.; Chen, C.; Wang, S.; Cheng, J.; Wu, Y. A high-entropy $V_{35}Ti_{35}Fe_{15}Cr_{10}Zr_5$ alloy with excellent high-temperature strength. *Mater. Des.* **2017**, *121*, 229–236. [CrossRef]
16. Lee, K.S.; Kang, J.-H.; Lim, K.R.; Na, Y.S. Influence of compressive strain on the microstructural evolution of an AlCoCrFeNi high entropy alloy. *Mater. Charact.* **2017**, *132*, 162–168. [CrossRef]
17. Jiang, S.; Sun, D.; Zhang, Y.; Wang, S.; Zhao, C. Plastic deformation mechanisms of equiatomic $Ni_{20}Ti_{20}Fe_{20}Al_{20}Cu_{20}$ high-entropy alloy at high temperatures. *J. Mater. Sci.* **2017**, *52*, 3199–3207. [CrossRef]
18. Wang, J.; Liu, Y.; Liu, B.; Wang, Y.; Cao, Y.; Li, T.; Zhou, R. Flow behavior and microstructures of powder metallurgical $CrFeCoNiMo_{0.2}$ high entropy alloy during high temperature deformation. *Mater. Sci. Eng. A* **2017**, *689*, 233–242. [CrossRef]
19. Zou, Y.; Sheeler, J.; Ma, H.; Okle, P.; Spolenak, R. Nanocrystalline high-entropy alloys: A new paradigm in high-temperature strength and stability. *Nano Lett.* **2017**, *17*, 1569–1574. [CrossRef]
20. Li, J.; Gao, B.; Tang, S.; Liu, B.; Liu, Y.; Wang, Y.; Wang, J. High temperature deformation behavior of carbon-containing FeCoCrNiMn high entropy alloy. *J. Alloys Compd.* **2018**, *747*, 571–579. [CrossRef]
21. Zhang, M.; Zhou, X.; Zhu, W.; Li, J. Influence of annealing on microstructure and mechanical properties of refractory $CoCrMoNbTi_{0.4}$ high-entropy alloy. *Metall. Mater. Trans. A* **2018**, *49*, 1313–1327. [CrossRef]
22. Rahul, M.; Samal, S.; Venugopal, S.; Phanikumar, G. Experimental and finite element simulation studies on hot deformation behaviour of $AlCoCrFeNi_{2.1}$ eutectic high entropy alloy. *J. Alloys Compd.* **2018**, *749*, 1115–1127. [CrossRef]
23. Eleti, R.R.; Bhattacharjee, T.; Zhao, L.; Bhattacharjee, P.P.; Tsuji, N. Hot deformation behavior of CoCrFeMnNi FCC high entropy alloy. *Mater. Chem. Phys.* **2018**, *210*, 176–186. [CrossRef]

24. Cao, Y.; Liu, Y.; Liu, B.; Zhang, W. Precipitation behavior during hot deformation of powder metallurgy Ti-Nb-Ta-Zr-Al high entropy alloys. *Intermetallics* **2018**, *100*, 95–103. [CrossRef]
25. Tong, Y.; Qiao, J.; Yao, Y. The constitutive model and threshold stress for characterizing the deformation mechanism of $Al_{0.3}CoCrFeNi$ high entropy alloy. *Mater. Sci. Eng. A* **2018**, *730*, 137–146. [CrossRef]
26. Yang, C.; Aoyagi, K.; Bian, H.; Chiba, A. Microstructure evolution and mechanical property of a precipitation-strengthened refractory high-entropy alloy HfNbTaTiZr. *Mater. Lett.* **2019**, *254*, 46–49. [CrossRef]
27. Jeong, H.; Park, H.; Park, K.; Na, T.; Kim, W. High-temperature deformation mechanisms and processing maps of equiatomic CoCrFeMnNi high-entropy alloy. *Mater. Sci. Eng. A* **2019**, *756*, 528–537. [CrossRef]
28. Málek, J.; Zýka, J.; Lukáč, F.; Čížek, J.; Kunčická, L.; Kocich, R. Microstructure and mechanical properties of sintered and heat-treated HfNbTaTiZr high entropy alloy. *Metals* **2019**, *9*, 1324. [CrossRef]
29. Tang, K.; Chen, L.; Wang, S.; Wei, R.; Yang, Z.; Jiang, F.; Sun, J. Development of a large size FCC high-entropy alloy with excellent mechanical properties. *Mater. Sci. Eng. A* **2019**, *761*, 138039. [CrossRef]
30. Annasamy, M.; Haghdadi, N.; Taylor, A.; Hodgson, P.; Fabijanic, D. Dynamic recrystallization behaviour of AlxCoCrFeNi high entropy alloys during high-temperature plane strain compression. *Mater. Sci. Eng. A* **2019**, *745*, 90–106. [CrossRef]
31. Kahnooji, M.; Zarei-Hanzaki, A.; Abedi, H.; Hassanpour-Esfahani, M.; Jalali, M.; Gubicza, J.; Heczel, A. An investigation into the dynamic recrystallization behavior of a non- equiatomic high entropy alloy. *Mater. Sci. Eng. A* **2019**, *768*, 138423. [CrossRef]
32. Prasad, N.; Bibhanshu, N.; Nayan, N.; Avadhani, G.; Suwas, S. Hot deformation behavior of the high-entropy alloy CoCuFeMnNi. *J. Mater. Res.* **2019**, *34*, 744–755. [CrossRef]
33. Eleti, R.; Bhattacharjee, T.; Shibata, A.; Tsuji, N. Unique deformation behavior and microstructure evolution in high temperature processing of HfNbTaTiZr refractory high entropy alloy. *Acta Mater.* **2019**, *171*, 132–145. [CrossRef]
34. Kim, W.; Jeong, H.; Park, H.; Park, K.; Na, T.; Choi, E. The effect of Al to high-temperature deformation mechanisms and processing maps of $Al_{0.5}CoCrFeMnNi$ high entropy alloy. *J. Alloys Compd.* **2019**, *802*, 152–165. [CrossRef]
35. Guo, W.; Liu, B.; Liu, Y.; Li, T.; Fu, A.; Fang, Q.; Nie, Y. Microstructures and mechanical properties of ductile NbTaTiV refractory high entropy alloy prepared by powder metallurgy. *J. Alloys Compd.* **2019**, *776*, 428–436. [CrossRef]
36. Xu, X.; Chen, S.; Ren, Y.; Hirata, A.; Fujita, T.; Liaw, P.; Chen, M. Temperature-dependent compression behavior of an Al0.5CoCrCuFeNi high-entropy alloy. *Materialia* **2019**, *5*, 100243. [CrossRef]
37. Wang, Y.; Li, J.; Xin, Y.; Li, C.; Cheng, Y.; Chen, X.; Rashad, M.; Liu, B.; Liu, Y. Effect of Zener–Hollomon parameter on hot deformation behavior of $CoCrFeMnNiC_{0.5}$ high entropy alloy. *Mater. Sci. Eng. A* **2019**, *768*, 138483. [CrossRef]
38. Wang, Y.-T.; Li, J.-B.; Xin, Y.-C.; Chen, X.-H.; Rashad, M.; Liu, B.; Liu, Y. Hot deformation behavior and hardness of a CoCrFeMnNi high-entropy alloy with high content of carbon. *Acta Metall. Sin.* **2019**, *32*, 932–943. [CrossRef]
39. Alijani, F.; Reihanian, M.; Gheisari, K.; Miyamoto, H. Microstructure and high-temperature deformation behavior of FeCoNiMnV high entropy alloy. *Mater. Chem. Phys.* **2020**, *256*, 123675. [CrossRef]
40. Dong, F.; Yuan, Y.; Li, W.; Zhang, Y.; Liaw, P.; Yuan, X.; Huang, H. Hot deformation behavior and processing maps of an equiatomic MoNbHfZrTi refractory high entropy alloy. *Intermetallics* **2020**, *126*, 106921. [CrossRef]
41. Aripov, G.R.; Bazlov, A.I.; Churyumov, A.Y.; Polkin, V.I.; Luzgin, D.V.; Prokoshkin, S.D. Study of the change in the structure and properties of high-entropic alloys during thermal and thermomechanical processing. *Russ. J. Non-Ferr. Met.* **2020**, *61*, 413–420. [CrossRef]
42. Jeong, H.; Park, H.; Kang, H.; Kim, W. Operation of solute-drag creep in an AlCoCrFeMnNi high-entropy alloy and enhanced hot workability. *J. Alloys Compd.* **2020**, *824*, 153829. [CrossRef]
43. Lin, L.; Xian, X.; Zhong, Z.; Chen, C.; Zhu, Z.; Wu, Y.; Liaw, P. A multi-phase $CrMnFeCoNiAl_{0.75}$ high-entropy alloy with high strength at intermediate temperature. *Intermetallics* **2020**, *120*, 106744. [CrossRef]
44. Hu, M.-L.; Song, W.-D.; Duan, D.-B.; Wu, Y. Dynamic behavior and microstructure characterization of TaNbHfZrTi high-entropy alloy at a wide range of strain rates and temperatures. *Int. J. Mech. Sci.* **2020**, *182*, 105738. [CrossRef]
45. Patnamsetty, M.; Somani, M.C.; Ghosh, S.; Ahmed, S.; Peura, P. Processing map for controlling microstructure and unraveling various deformation mechanisms during hot working of CoCrFeMnNi high entropy alloy. *Mater. Sci. Eng. A* **2020**, *793*, 139840. [CrossRef]
46. Patnamsetty, M.; Saastamoinen, A.; Somani, M.C.; Peura, P. Constitutive modelling of hot deformation behaviour of a CoCrFeMnNi high-entropy alloy. *Sci. Technol. Adv. Mater.* **2020**, *21*, 43–55. [CrossRef] [PubMed]
47. Ahmed, M.Z.; Chadha, K.; Reddy, S.R.; Shahriari, D.; Bhattacharjee, P.P.; Jahazi, M. Influence of process parameters on microstructure evolution during hot deformation of a eutectic high-entropy alloy (EHEA). *Metall. Mater. Trans. A* **2020**, *51*, 6406–6420. [CrossRef]
48. Haghdadi, N.; Primig, S.; Annasamy, M.; Cizek, P.; Hodgson, P.; Fabijanic, D. Dynamic recrystallization in AlXCoCrFeNi duplex high entropy alloys. *J. Alloys Compd.* **2020**, *830*, 154720. [CrossRef]
49. Haghdadi, N.; Primig, S.; Annasamy, M.; Cizek, P.; Hodgson, P.D.; Fabijanic, D.M. On the hot-worked microstructure of a face-centered cubic Al0.3CoCrFeNi high entropy alloy. *Scr. Mater.* **2020**, *178*, 144–149. [CrossRef]
50. Senkov, O.N.; Couzinie, J.P.; Rao, S.I.; Soni, V.; Banerjee, R. Temperature dependent deformation behavior and strengthening mechanisms in a low density refractory high entropy alloy $Al_{10}Nb_{15}Ta_5Ti_{30}Zr_{40}$. *Materialia* **2020**, *9*, 100627. [CrossRef]
51. Tian, Q.; Zhang, G.; Yin, K.; Wang, L.; Wang, W.; Cheng, W.; Wang, Y.; Huang, J.C. High temperature deformation mechanism and microstructural evolution of relatively lightweight AlCoCrFeNi high entropy alloy. *Intermetallics* **2020**, *119*, 106707. [CrossRef]

52. Jain, R.; Rahul, M.; Samal, S.; Kumar, V.; Phanikumar, G. Hot workability of CoeFeeMneNieTi eutectic high entropy alloy. *J. Alloys Compd.* **2020**, *822*, 153609. [CrossRef]
53. Cao, T.; Ma, L.; Wang, L.; Zhou, J.; Wang, Y.; Wang, B.; Xue, Y. High temperature deformation behavior of dual-phase $Al_{0.6}CoCrFeNi$ high-entropy alloys. *J. Alloys Compd.* **2020**, *836*, 155305. [CrossRef]
54. Jain, R.; Jain, A.; Rahul, M.R.; Kumar, A.; Dubey, M.; Sabat, R.K.; Samal, S.; Phanikumar, G. Development of ultrahigh strength novel Co–Cr–Fe–Ni–Zr quasi-peritectic high entropy alloy by an integrated approach using experiment and simulation. *Materialia* **2020**, *14*, 100896. [CrossRef]
55. Eleti, R.R.; Chokshi, A.H.; Shibata, A.; Tsuji, N. Unique high-temperature deformation dominated by grain boundary sliding in heterogeneous necklace structure formed by dynamic recrystallization in HfNbTaTiZr BCC refractory high entropy alloy. *Acta Mater.* **2020**, *183*, 64–77. [CrossRef]
56. Wang, X.; Zhang, Y.; Ma, X. High temperature deformation and dynamic recrystallization behavior of AlCrCuFeNi high entropy alloy. *Mater. Sci. Eng. A* **2020**, *778*, 139077. [CrossRef]
57. Kim, Y.K.; Yang, S.; Lee, K.A. Superior temperature-dependent mechanical properties and deformation behavior of equiatomic CoCrFeMnNi high-entropy alloy additively manufactured by selective laser melting. *Sci. Rep.* **2020**, *10*, 8045. [CrossRef]
58. Brown, C.; McCarthy, T.; Chadha, K.; Rodrigues, S.; Aranas, C., Jr.; Saha, G. Constitutive modeling of the hot deformation behavior of CoCrFeMnNi high-entropy alloy. *Mater. Sci. Eng. A* **2021**, *826*, 141940. [CrossRef]
59. Watanabe, H.; Murata, T.; Ikeo, N.; Mukai, T.; Han, K.; Tsuchiya, K. Effect of initial microstructure on grain refinement under hot compression in CrMnFeCoNi high-entropy alloy with Al addition. *Materialia* **2021**, *18*, 101172. [CrossRef]
60. Yi, H.; Wei, D.; Xie, R.; Zhang, Y.; Kato, H. Microstructure refinement of a transformation-induced plasticity high-entroy alloy. *Materials* **2021**, *14*, 1196. [CrossRef]
61. Yi, H.; Zhang, Y.; Xie, R.; Bi, M.; Wei, D. High-temperature deformation behaviors of the C-doped and N-doped high entropy alloys. *Metals* **2021**, *11*, 1517. [CrossRef]
62. Jeong, H.T.; Kim, W.J. Calculation and construction of deformation mechanism maps and processing maps for CoCrFeMnNi and $Al_{0.5}CoCrFeMnNi$ high-entropy alloys. *J. Alloys Compd.* **2021**, *869*, 159256. [CrossRef]
63. Jeong, H.T.; Park, H.K.; Kim, W.J. Dynamic recrystallization and hot deformation mechanisms of a eutectic $Al_{0.7}CoCrFeMnNi$ high-entropy alloy. *J. Alloys Compd.* **2021**, *871*, 159488. [CrossRef]
64. Jeong, H.T.; Park, H.K.; Kim, W.J. Hot deformation behavior and processing map of a $Sn_{0.5}CoCrFeMnNi$ high entropy alloy with dual phases. *Mater. Sci. Eng. A* **2021**, *801*, 140394. [CrossRef]
65. Yasuda, H.Y.; Yamada, Y.; Cho, K.; Nagase, T. Deformation behavior of HfNbTaTiZr high entropy alloy singe crystals and polycrystals. *Mater. Sci. Eng. A* **2021**, *809*, 140983. [CrossRef]
66. Jiang, J.; Huang, M.; Wang, Y.; Xiao, G.; Liu, Y.; Zhang, Y. Unique hot deformation behavior and microstructure evolution of a dual FCC-phase $CoCrCu_{1.2}FeNi$ high entropy alloy. *J. Alloys Compd.* **2021**, *876*, 160102. [CrossRef]
67. Xu, L.; Chen, Z.; Zheng, Y.; Wang, X.; Han, S.; Xiao, S.; Chen, Y. Deformation behavior and microstructure evolution of as-cast $Ti_2ZrMo_{0.5}Nb_{0.5}$ high entropy alloy. *J. Mater. Res. Technol.* **2021**, *13*, 2469–2481. [CrossRef]
68. Wang, M.; Ma, Z.; Xu, Z.Q.; Cheng, X.W. Effects of vanadium concentration on mechanical properties of VxNbMoTa refractory high-entropy alloys. *Mater. Sci. Eng. A* **2021**, *808*, 140848. [CrossRef]
69. Wang, M.; Lu, Y.; Wang, T.; Zhang, C.; Cao, Z.; Li, T.; Liaw, P.K. A novel bulk eutectic high-entropy alloy with outstanding as-cast specific yield strengths at elevated temperatures. *Scr. Mater.* **2021**, *204*, 114132. [CrossRef]
70. Shah, N.; Rahul, M.; Bysakh, S.; Phanikumar, G. Microstructure stability during high temperature deformation of CoCrFeNiTa eutectic high entropy alloy through nano-scale precipitation. *Mater. Sci. Eng. A* **2021**, *824*, 141793. [CrossRef]
71. Liu, Q.; Wang, G.; Liu, Y.; Sui, X.; Chen, Y.; Luo, S. Hot deformation behaviors of an ultrafine-grained MoNbTaTiV refractory high-entropy alloy fabricated by powder metallurgy. *Mater. Sci. Eng. A* **2021**, *809*, 140922. [CrossRef]
72. Wang, Q.; Gao, T.; Du, H.; Hu, Q.; Chen, Q.; Fan, Z.; Zeng, L.; Liu, X. Hot compression behaviors and microstructure evolutions of a cast dual-phase $NiCoFeCrA_{l0.7}$ high-entropy alloy. *Intermetallics* **2021**, *138*, 107314. [CrossRef]
73. Jain, R.; Rahul, M.R.; Chakraborty, P.; Sabat, R.K.; Samal, S.; Phanikumar, G.; Tewari, R. Design and deformation characteristics of single-phase Co-Cr-Fe-Ni-V high entropy alloy. *J. Alloys Compd.* **2021**, *888*, 161579. [CrossRef]
74. Cao, T.; Guo, W.; Lu, W.; Xue, Y.; Lu, W.; Su, J.; Liebscher, C.H.; Li, C.; Dehm, G. Strain rate dependent deformation behavior of BCC-structured $Ti_{29}Zr_{24}Nb_{23}Hf_{24}$ high entropy alloy at elevated temperatures. *J. Alloys Compd.* **2021**, *891*, 161859. [CrossRef]
75. Lee, U.; Straumal, B.; Park, N. Dynamic precipitation of σ-phase and element partitioning in equiatomic CoCrFeMnNi high-entropy alloy. *Mater. Sci. Eng. A* **2021**, *804*, 140739. [CrossRef]
76. Nie, X.W.; Cai, M.D.; Cai, S. Microstructure and mechanical properties of a novel refractory high entropy alloy HfMoScTaZr. *Int. J. Refract. Hard Met.* **2021**, *98*, 105568. [CrossRef]
77. Cao, Y.; Zhang, W.; Liu, B.; Liu, Y.; Du, M.; Fu, A. Phase decomposition behavior and its effects on mechanical properties of $TiNbTa_{0.5}ZrAl_{0.5}$ refractory high entropy alloy. *J. Mater. Sci. Technol.* **2021**, *66*, 10–20. [CrossRef]
78. Guo, Y.; He, J.; Lu, W.; Jia, L.; Li, Z. The evolution of compositional and microstructural heterogeneities in a $TaMo_{0.5}ZrTi_{1.5}Al_{0.1}Si_{0.2}$ high entropy alloy. *Mater. Charact.* **2021**, *172*, 110836. [CrossRef]
79. Bai, Z.C.; Ding, X.F.; Hu, Q.; Yang, M.; Fan, Z.T.; Liu, X.W. Unique deformation behavior and microstructure evolution in high-temperature processing of a low-density $TiAlVNb_2$ refractory high-entropy alloy. *J. Alloys Compd.* **2021**, *885*, 160962. [CrossRef]

80. Kaypour, H.; Nategh, S.; Gholamipour, R.; Khodabandeh, A. High-temperature compressive behavior and kinetics analysis of $Al_{0.4}MnCrCoFeNi$ high entropy alloy. *Mater. Res. Express* **2021**, *8*, 066505. [CrossRef]
81. Wang, J.; Li, H.; Yang, H.; Zhang, Y.; Wang, W.Y.; Li, J. Hot deformation and subsequent annealing on the microstructure and hardness of an $Al_{0.3}CoCrFeNi$ high-entropy alloy. *Acta Metall. Sin.* **2021**, *34*, 1527–1536. [CrossRef]
82. Lin, L.; Xian, X.; Zhong, Z.; Song, K.; Wang, C.; Wang, G.; Wu, Y.; Liaw, P.K. Microstructure and compression properties of a dual-phase FeCoCrMn high-entropy alloy. *Adv. Compos. Hybrid Mater.* **2022**, *5*, 1508–1515. [CrossRef]
83. Chanda, B.; Pani, S.K.; Das, J. Mechanism of microstructure evolution and spheroidization in ultrafine lamellar $CoCrFeNi(Nb_{0.5}/Ta_{0.4})$ eutectic high entropy alloys upon hot deformation. *Mater. Sci. Eng. A* **2022**, *835*, 142669. [CrossRef]
84. Emdadi, A.; Stryzhyboroda, O.; Hecht, U.; Bambach, M. Complex dynamic restoration processes leading to a high degree of deformability in a dual-phase $Al_{0.5}CoCrFeNi$ high entropy alloy. *J. Alloys Compd.* **2022**, *918*, 165583. [CrossRef]
85. De Freitas, C.C.; Caram, R.; Campo, K.N. Semisolid deformation behavior and processing of CoCrCuxFeNi high-entropy alloys. *Intermetallics* **2022**, *150*, 107682. [CrossRef]
86. Ge, S.; Lin, S.; Fu, H.; Zhang, L.; Geng, T.; Zhu, Z.; Li, Z.; Li, H.; Wang, A.; Zhang, H.; et al. High-temperature Mechanical Properties and Dynamic Recrystallization Mechanism of in situ Silicide-reinforced MoNbTaTiVSi Refractory High-entropy Alloy Composite. *Acta Metall. Sin.* **2022**, *35*, 1617–1630. [CrossRef]
87. Jain, R.; Umre, P.; Sabat, R.K.; Kumar, V.; Samal, S. Constitutive and artificial neural network modeling to predict hot deformation behavior of CoFeMnNiTi eutectic high-entropy alloy. *J. Mater. Eng. Perform.* **2022**, *31*, 8124–8135. [CrossRef]
88. Li, T.; Lu, Y.; Li, Z.; Wang, T.; Li, T. Hot deformation behavior and microstructure evolution of non-equimolar $Ti_2ZrHfV_{0.5}Ta_{0.2}$ refractory high-entropy alloy. *Intermetallics* **2022**, *146*, 107586. [CrossRef]
89. Liu, X.R.; He, F.; Li, J.J.; Dang, Y.Y.; Wang, Z.J.; Wang, J.C. Tailoring microstructures of $CoCrFeNiNb_{0.25}$ hypoeutectic high-entropy alloy by hot deformation. *Rare Met.* **2022**, *41*, 2028–2037. [CrossRef]
90. Marzbali, M.H.; Jafarian, H.R.; Bokaei, S.; Park, N.; Momeni, A.; Eivani, A.R. On the microstructure and mechanical properties of FeCoCrCuNi high entropy alloy during hot compression. *J. Mater. Res. Technol.* **2022**, *16*, 1747–1760. [CrossRef]
91. Mei, J.; Wu, T.; Wei, N.; Xue, F.; Cai, Z.; Xue, X. Hot compression behavior of a novel high entropy alloy. *Metals* **2022**, *12*, 463. [CrossRef]
92. Patnamsetty, M.; Ghosh, S.; Somani, M.C.; Peura, P. Characterization of hot deformation behavior of $Al_{0.3}CoCrFeNi$ high-entropy alloy and development of processing map. *J. Alloys Compd.* **2022**, *914*, 165341. [CrossRef]
93. Qiao, L.; Zhu, J. Constitutive modeling of hot deformation behavior of AlCrFeNi multi-component alloy. *Vacuum* **2022**, *201*, 111059. [CrossRef]
94. Qu, S.; Fang, Y.; Liang, J.; Zheng, J.H.; Zheng, K. A physical mechanism-based model of CoCrFeMnNi high entropy alloy considering adiabatic heat effect for hot bulk forming processes. *Metals* **2022**, *12*, 1011. [CrossRef]
95. Sajadi, S.A.; Toroghinejad, M.R.; Rezaeian, A.; Ebrahimi, G.R. A study of hot compression behavior of an as-cast $FeCrCuNi_2Mn_2$ high-entropy alloy. *J. Alloys Compd.* **2022**, *896*, 162732. [CrossRef]
96. Sajadi, S.A.; Toroghinejad, M.R.; Rezaeian, A.; Ebrahimi, G.R. Dynamic recrystallization behavior of the equiatomic FeCoCrNi high-entropy alloy during high temperature deformation. *J. Mater. Res. Technol.* **2022**, *20*, 1093–1109. [CrossRef]
97. Wang, J.; Yang, P.; Wang, D. Constitutive equation and microstructure analysis of $Al_{0.6}CoCrFeNi$ high entropy alloy during hot deformation. *Philos. Mag.* **2022**, *102*, 1684–1707. [CrossRef]
98. Wu, S.; Qiao, D.; Zhang, H.; Miao, J.; Zhao, H.; Wang, J.; Lu, Y.; Wang, T.; Li, T. Microstructure and mechanical properties of $CxHf_{0.25}NbTaW_{0.5}$ refractory high-entropy alloys at room and high temperatures. *J. Mater. Sci. Technol.* **2022**, *97*, 229–238. [CrossRef]
99. Yu, Z.; Xie, B.; Zhu, Z.; Xu, B.; Sun, M. High-temperature deformation behavior and processing maps of a novel $AlNbTi_3VZr_{1.5}$ refractory high entropy alloy. *J. Alloys Compd.* **2022**, *912*, 165220. [CrossRef]
100. John, R.; Dash, M.K.; Murty, B.S.; Fabijanic, D. Effect of temperature and strain rate on the deformation behaviour and microstructure of $Al_{0.7}CoCrFeNi$ high entropy alloy. *Mater. Sci. Eng. A* **2022**, *856*, 143933. [CrossRef]
101. Prasad, Y.V.R.K.; Rao, K.P.; Sasidhara, S. *Hot Working Guide: A Compendium of Processing Maps*, 2nd ed.; ASM International: Materials Park, OH, USA, 2015.
102. Wang, W.R.; Wang, W.L.; Wang, S.C.; Tsai, Y.C.; Lai, C.H.; Yeh, J.W. Effects of Al addition on the microstructure and mechanical property of AlxCoCrFeNi high-entropy alloys. *Intermetallcs* **2012**, *26*, 44–51. [CrossRef]
103. He, J.Y.; Liu, W.H.; Wang, H.; Wu, Y.; Liu, X.J.; Nieh, T.G.; Lu, Z.P. Effects of Al addition on structural evolution and tensile properties of the FeCoNiCrMn high-entropy alloy system. *Acta Mater.* **2014**, *62*, 105–113. [CrossRef]
104. Garofalo, F. An empirical relation defining the stress dependence of minimum creep rate in metals. *Trans. AIME* **1963**, *227*, 351–356.
105. Nabarro, F.R.N. Report of the Conference on the Strength of Solids, London. *Phys. Soc.* **1948**, 75–81.
106. Herring, C. Diffusional viscosity of a polycrystalline solid. *J. Appl. Phys.* **1950**, *21*, 437–445. [CrossRef]
107. Coble, R.L. A model for boundary diffusion controlled creep in polycrystalline materials. *J. Appl. Phys.* **1963**, *34*, 1679–1682. [CrossRef]
108. Harper, J.; Dorn, J.E. Viscous creep of aluminum near its melting temperature. *Acta Metall.* **1957**, *5*, 654–665. [CrossRef]
109. Lüthy, H.; White, R.; Sherby, O.D. Grain boundary sliding and deformation mechanism maps. *Mater. Sci. Eng.* **1979**, *39*, 211–216. [CrossRef]

110. Ruano, O.A.; Miller, A.K.; Sherby, O.D. The influence of pipe diffusion on the creep of fine-grained materials. *Mater. Sci. Eng.* **1981**, *51*, 9–16. [CrossRef]
111. Hong, S.H.; Weertman, J. High temperature creep of ordered and disordered beta brass—II. Internal stress. *Acta Metall.* **1986**, *34*, 743–751. [CrossRef]
112. Robinson, S.H.; Sherby, O.D. Mechanical behavior of polycrystalline tungsten at elevated temperature. *Acta Metall.* **1969**, *17*, 109–125. [CrossRef]
113. Ruano, O.A.; Wadsworth, J.; Sherby, O.D. Deformation mechanisms in an austenitic stainless steel (25Cr-20Ni) at elevated temperature. *J. Mater. Sci.* **1985**, *20*, 3735–3744. [CrossRef]
114. Zhang, Y.; Yang, X.; Liaw, P.K. Alloy design and properties optimization of high-entropy alloys. *JOM* **2012**, *64*, 830–838.
115. Vaidya, M.; Pradeep, K.G.; Murty, B.S.; Wilde, G.; Divinski, S.V. Bulk tracer diffusion in CoCrFeNi and CoCrFeMnNi high entropy alloys. *Acta Mater.* **2018**, *146*, 211–224. [CrossRef]
116. Li, Q.; Chen, W.; Zhong, J.; Zhang, Q.; Liu, Z.K. On sluggish diffusion in fcc Al-Co-Cr-Fe-Ni high-entropy alloys: An expermental and numerical study. *Metals* **2018**, *8*, 16. [CrossRef]
117. Frost, H.J.; Ashby, M.F. *Deformation Mechanism Maps*; Pergamon Press: Oxford, UK, 1983.
118. Murty, S.V.S.N.; Sarma, M.S.; Rao, B.N. On the evaluation of efficiency parameters in processing maps. *Metall. Mater. Trans.* **1997**, *28*, 1581–1582. [CrossRef]
119. Murty, S.V.S.N.; Rao, B.N. On the development of instability criteria during hot working with reference to IN 718. *Mater. Sci. Eng. A* **1998**, *254*, 76–82. [CrossRef]
120. Kim, W.J.; Jeong, H.T. Easy construction of processing maps for metallic alloys using a flow instability criterion based on power-law breakdown. *J. Mater. Res. Technol.* **2020**, *9*, 5134–5143. [CrossRef]
121. Jeong, H.T.; Han, S.H.; Kim, W.J. Effects of large amounts of Mg (5–13 wt%) on hot compressive deformation behavior and processing maps of Al-Mg alloys. *J. Alloys Compd.* **2019**, *788*, 1282–1299. [CrossRef]